



# The Hydrogen-poor Superluminous Supernovae from the Zwicky Transient Facility Phase I Survey. II. Light-curve Modeling and Characterization of Undulations

Z. H. Chen<sup>1</sup>, Lin Yan<sup>2</sup>, T. Kangas<sup>3</sup>, R. Lunnan<sup>4</sup>, J. Sollerman<sup>4</sup>, S. Schulze<sup>5</sup>, D. A. Perley<sup>6</sup>, T.-W. Chen<sup>4</sup>, K. Taggart<sup>7</sup>, K. R. Hinds<sup>6</sup>, A. Gal-Yam<sup>8</sup>, X. F. Wang<sup>1,9</sup>, K. De<sup>10</sup>, E. Bellm<sup>11</sup>, J. S. Bloom<sup>12,13</sup>, R. Dekany<sup>2</sup>, M. Graham<sup>10</sup>, M. Kasliwal<sup>14</sup>, S. Kulkarni<sup>14</sup>, R. Laher<sup>15</sup>, D. Neill<sup>10</sup>, and B. Rusholme<sup>15</sup>

<sup>1</sup> Physics Department and Tsinghua Center for Astrophysics (THCA), Tsinghua University, Beijing, 100084, People's Republic of China  
chenzh18@mails.tsinghua.edu.cn

<sup>2</sup> Caltech Optical Observatories, California Institute of Technology, Pasadena, CA 91125, USA; [lyan@caltech.edu](mailto:lyan@caltech.edu)

<sup>3</sup> The Oskar Klein Centre, KTH Royal Institute of Technology, Stockholm, Sweden

<sup>4</sup> The Oskar Klein Centre, Department of Astronomy, Stockholm University, AlbaNova, SE-106 91 Stockholm, Sweden

<sup>5</sup> The Oskar Klein Centre, Department of Physics, Stockholm University, AlbaNova, SE-106 91 Stockholm, Sweden

<sup>6</sup> Astrophysics Research Institute, Liverpool John Moores University, 146 Brownlow Hill, Liverpool L3 5RF, UK

<sup>7</sup> Department of Astronomy and Astrophysics, University of California, Santa Cruz, CA 95064, USA

<sup>8</sup> Department of particle physics and astrophysics, Weizmann Institute of Science, 76100 Rehovot, Israel

<sup>9</sup> Beijing Planetarium, Beijing Academy of Sciences and Technology, Beijing, 100044, People's Republic of China

<sup>10</sup> Cahill Center for Astrophysics, California Institute of Technology, 1200 E. California Blvd. Pasadena, CA 91125, USA

<sup>11</sup> DIRAC Institute, Department of Astronomy, University of Washington, 3910 15th Avenue NE, Seattle, WA 98195, USA

<sup>12</sup> Department of Astrophysics, University of California, Berkeley, CA 94720-3411, USA

<sup>13</sup> Lawrence Berkeley National Laboratory, 1 Cyclotron Road, MS 50B-4206, Berkeley, CA 94720, USA

<sup>14</sup> Division of Physics, Mathematics, and Astronomy, California Institute of Technology, Pasadena, CA 91125, USA

<sup>15</sup> IPAC, California Institute of Technology, 1200 E. California Blvd, Pasadena, CA 91125, USA

Received 2022 February 2; revised 2022 October 31; accepted 2022 October 31; published 2023 January 24

## Abstract

We present analysis of the light curves (LCs) of 77 hydrogen-poor superluminous supernovae (SLSNe I) discovered during the Zwicky Transient Facility Phase I operation. We find that the majority (67%) of the sample can be fit equally well by both magnetar and ejecta–circumstellar medium (CSM) interaction plus  $^{56}\text{Ni}$  decay models. This implies that LCs alone cannot unambiguously constrain the physical power sources for an SLSN I. However, 23% of the sample show inverted V-shape, steep-declining LCs or features of long rise and fast post-peak decay, which are better described by the CSM+Ni model. The remaining 10% of the sample favors the magnetar model. Moreover, our analysis shows that the LC undulations are quite common, with a fraction of 18%–44% in our gold sample. Among those strongly undulating events, about 62% of them are found to be CSM-favored, implying that the undulations tend to occur in the CSM-favored events. Undulations show a wide range in energy and duration, with median values (and  $1\sigma$  errors) being as  $1.7\%_{-0.7\%}^{+1.5\%} E_{\text{rad, total}}$  and  $28.8_{-9.1}^{+14.4}$  days, respectively. Our analysis of the undulation timescales suggests that intrinsic temporal variations of the central engine can explain half of the undulating events, while CSM interaction (CSI) can account for the majority of the sample. Finally, all of the well-observed He-rich SLSNe Ib either have strongly undulating LCs or the LCs are much better fit by the CSM+Ni model. These observations imply that their progenitor stars have not had enough time to lose all of the He-envelopes before supernova explosions, and H-poor CSM are likely to present in these events.

*Unified Astronomy Thesaurus concepts:* Supernovae (1668)

*Supporting material:* machine-readable tables

## 1. Introduction

Superluminous supernovae (SLSNe), as one group of energetic stellar explosions, were first discovered in the mid-2000s (Ofek et al. 2007; Quimby et al. 2007; Smith et al. 2007). They are 10–100 times more luminous at the peak phase and evolve much slower than normal Type Ia and core-collapse supernovae (SNe). After the initial discoveries, it quickly became clear that the conventional radioactive decay model for normal core-collapse supernovae (CCSNe) cannot explain the majority of SLSNe. Today, what powers these luminous and slowly evolving events remains unclear. Several mechanisms

have been proposed, including interaction with circumstellar medium (CSM; Chevalier & Irwin 2011; Chatzopoulos et al. 2012, 2013; Benetti et al. 2014), energy injection from a central engine such as a rapidly rotating neutron star (magnetar, Kasen & Bildsten 2010; Woosley 2010), or an accreting black hole (Dexter & Kasen 2013). Exotic, rare explosions were also proposed, such as electron–positron pair-instability supernovae (PISNe) or pulsational PISNe (PPISNe) theoretically predicted for extremely massive stars (Barkat et al. 1967; Rakavy & Shaviv 1967; Woosley et al. 2007; Woosley 2017).

Magnetar models are flexible and often used to fit the light curves (LCs) of SLSNe I (e.g., Ingersoll et al. 2013; Nicholl et al. 2013). However, some observations already indicate that magnetar spin-down is not the only process that affects the LC luminosity and morphology for an SLSN I, and there might be multiple processes affecting the optical emission. For example,



Original content from this work may be used under the terms of the [Creative Commons Attribution 4.0 licence](https://creativecommons.org/licenses/by/4.0/). Any further distribution of this work must maintain attribution to the author(s) and the title of the work, journal citation and DOI.

the detection of late-time  $H\alpha$  emission in three SLSNe I indicates the presence of H-rich CSM shells ejected by the progenitor stars (Yan et al. 2015, 2017a). Another example is the discovery of Mg II emission lines resonant scattered by a H-poor CSM shell in the SLSN I PTF16eh (Lunnan et al. 2018). Finally, the sharp V-shaped LCs of SN 2017egm are shown to be better fit by the ejecta–CSI model (Wheeler et al. 2017). Statistically, it is not clear what roles magnetars and CSI play for the population of SLSNe I, and this needs further studies.

Temporal bumps or dips in SLSN I LCs are known and have been observed in various objects (Nicholl et al. 2016; Yan et al. 2017a, 2017b; Anderson et al. 2018; Lunnan et al. 2020). LCs with such undulations cannot be explained by a simple magnetar model or CSI model. Previously, poor LC sampling and lack of uniform SLSN I data sets have precluded detailed statistical analysis of LC undulations. A recent paper by Hosseinzadeh et al. (2022, cited as H22 hereafter) has carried out a focused study using the published SLSN I LCs from the literature. It discussed various possible physical drivers for this phenomenon but found no conclusive answers. The H22 sample is compiled from multiple sources, which can introduce biases to undulation fractions and properties. The Zwicky Transient Facility (ZTF) Phase I survey (Bellm et al. 2019a; Graham et al. 2019; Masci et al. 2019) has discovered and classified a large sample of SLSNe I. The advantages of the ZTF LCs are the high cadence (3 days or less) and the excellent phase coverage at both early and late times (Bellm et al. 2019b). This provides a valuable opportunity to perform a statistical study on the LC undulations.

The description of the ZTF survey, the SLSN I sample, and the complete photometric data set are published in Chen et al. (2022), Paper I of this series. Paper I presented mostly the parameters that can be measured or directly computed from the data, such as redshift, extinction correction, K-correction, peak luminosity, peak phase, timescales (rise and decline), color, blackbody temperature, and bolometric luminosity.

This paper, Paper II, presents the detailed analysis of the LCs of the 77 of 78 ZTF SLSNe I published in Paper I, excluding SN 2018ibb. The LC and detailed analysis of SN 2018ibb will be published in Schulze et al. (in preparation). These are well-sampled events with evident undulations, and excluding them lowers our undulation fraction for about 2%. We focus on the LC morphology and various physical parameters derived from modeling, such as ejecta mass and explosion energy. Throughout the paper, apparent magnitudes are in the AB system, unless specified otherwise. We adopt a  $\Lambda$ CDM cosmology with  $H_0 = 70.0 \text{ km s}^{-1} \text{ Mpc}^{-1}$ ,  $\Omega_M = 0.3$ , and  $\Omega_\Lambda = 0.7$ .

## 2. The Data

Our sample contains 77 SLSNe I discovered from 2018 March 17 to 2020 October 31 by the ZTF survey. This sample covers redshifts of  $z \sim 0.06\text{--}0.67$ . The photometry data primarily comes from the ZTF in the  $g$ ,  $r$ ,  $i$  bands (Bellm et al. 2019a), and also includes additional data from other ground-based facilities (see Paper I for details) and Swift (Roming et al. 2005). Each event has been spectroscopically classified as described in Paper I. The majority of the spectra used for the velocity measurements are from the Double Beam Spectrograph (Oke & Gunn 1983) and the Low Resolution Imaging Spectrometer (Oke et al. 1995) mounted on the Palomar 200 inch (P200) and the Keck telescope respectively.

The spectra used for a velocity measurement but not presented in Paper I will be published in our future work.

We divide the ZTF SLSN I sample into three subsets—*gold*, *silver*, and *bronze*. This is because the undulations can be missed without sufficiently sampled data, and some results (e.g., the fraction of undulating events in Section 4.2) strongly depend on the LC phase coverage. The bronze class is defined as having  $g$ - and  $r$ -band LCs consisting of data points  $\leq 10$  epochs. The gold class is defined by the following two criteria: [1] no gap longer than 20 days in rest frame, but very late-time gaps (i.e., taken at 100 days after the peak or 2 mag fainter than the peak) are allowed; [2] the LC covers phases that reach at least 0.5 and 1.0 mag below the peak luminosity pre- and post-peak, respectively. The gold class has 40 SLSNe I, and the bronze class has only 4. The remaining 33 events are in the silver class whose LCs have  $>10$  epochs in either  $g$  or  $r$  band, but do not meet both gold class criteria. Some analysis is performed only with the LCs in the *gold* and *silver* classes.

## 3. Light-curve Modeling

### 3.1. Velocity Measurements at Peak Phases

The width of a bolometric LC is closely related to the effective diffusion timescale, which describes the time photons take to travel through the ejecta material and is proportional to  $(M_{\text{ej}}/V_{\text{ej}})^{1/2}$ . When modeling LCs to derive ejecta masses and other physical parameters, it reduces the number of free parameters and uncertainties if  $V_{\text{ej}}$  can be constrained separately from optical spectra. Here  $V_{\text{ej}}$  is approximated with the photospheric velocity at peak phases (Arnett 1982; Kasen & Bildsten 2010; Nicholl et al. 2017a).

We use three different ways to measure the photospheric velocities. The first method is to use Fe II  $\lambda\lambda 4924, 5018, 5169$  absorption lines as tracers. Liu et al. (2016), Modjaz et al. (2016) have shown that this method can derive robust measurements for stripped-envelope SNe, and the spectral template-matching technique can mitigate the blended Fe II lines for high-velocity events such as SNe Ic-BL. The second type of spectral tracers is the five O II absorption lines at 3737–4650 Å, the hallmark features for SLSNe I at early phases (Quimby et al. 2011). These are useful for velocity measurements as shown by Quimby et al. (2018), Gal-Yam (2019). The third method is to cross-correlate the spectra of our events with spectral templates from several well-studied SLSNe I, and estimate the relative spectral shifts, thus their relative velocities.

When measuring the velocities, the spectra are first cleaned by removing the narrow host emission lines, smoothed, and divided by the continua. Using the template-matching code SESNspectraLib<sup>16</sup> (Bianco et al. 2016; Liu et al. 2016; Modjaz et al. 2016), we measure 51 velocities with errors from Markov Chain Monte Carlo (MCMC) for 33 SLSNe I using Fe II features. Note that the pre-peak Fe II velocity can be underestimated due to the contamination of Fe III as illustrated in Liu et al. (2017b). And the post-peak Fe II velocity can be overestimated by about 9000  $\text{km s}^{-1}$  due to the blending effect of Fe II  $\lambda\lambda 4924, 5018$  and Fe II  $\lambda 5169$  (Quimby et al. 2018). We excluded those ambiguous measurements with velocities  $>15,000 \text{ km s}^{-1}$  and only one broad absorption component

<sup>16</sup> <https://github.com/nyusngroup/SESNspectraLib>

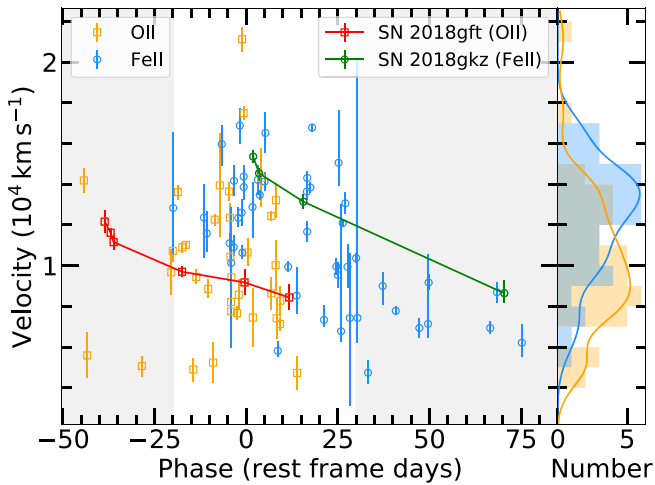


**Figure 1.** Photospheric velocities vs. phases. Fe II and O II velocities are marked with circles and squares, respectively. We mark the early (phase  $< -20$  days) and late (phase  $> +30$  days) time region with shaded area. The velocity evolutions of two events with good phase coverage are highlighted in different colors. The right panel shows the distribution of Fe II and O II velocities near peak phases in the white area. The blue and orange solid lines show the kernel density estimation of the distributions, respectively.

near the Fe II absorption features. When measuring O II, we derive the spectral shifts by fitting the local minima using the least-squares method, assuming the five absorption features have the same velocity. The errors are calculated from the covariance matrix. The five O II features do not have the same strength, with O II  $\lambda\lambda 4358, 4651$  (features A & B) being the strongest. For some spectra, we fit only 2 to 4 significant features because the others are too weak. We derive 41 velocities at phases  $-43$  to  $+14$  days for 33 SLSNe I using O II tracers. SN 2018gft has very strong O II features from  $-38.6$  to  $+11.7$  days, and we highlight its evolution in Figure 1.

For six events (namely SN 2018kyt, SN 2019ujb, SN 2019zbv, SN 2019aamr, SN 2019aamt, and SN 2020afag) in our sample, their O II lines are not clearly identified, especially when Mg I  $\lambda\lambda 3829, 3832, 3838$  or Ca II  $\lambda\lambda 3934, 3969$  may be present. For these spectra with ambiguous O II feature identifications, we match them with three well-observed SLSNe I, PTF12dam, SN 2011ke, and SN 2015bn near peak phases (Inserra et al. 2013; Nicholl et al. 2013, 2016; Quimby et al. 2018). We record the velocities derived from the five best-matching templates and use their mean value as our final result and the standard deviation as the error.

In total, we are able to measure photospheric velocities near peak phases for 51 events. The remaining events do not show clear Fe II or O II features or do not have sufficient spectra at the right phases. The measured velocities  $V_{ph}$  are listed in Table A1.

Figure 1 shows the measured velocities as a function of phase as well as the histograms of velocity distributions. The shaded region marks the early (phase  $< -20$  days) and late (phase  $> +30$  days) time region. The histogram distributions in the right panel show that, near the LC peak ( $-20$  days  $\lesssim$  phase  $\lesssim +30$  days), the Fe II velocity has a median value of  $12,800 \text{ km s}^{-1}$ , whereas the median O II velocity is only  $9700 \text{ km s}^{-1}$ . Considering the velocities from both ionic species, the median peak photospheric velocity is about  $10,900 \text{ km s}^{-1}$  for our sample of SLSNe I. A similar trend is found for PTF12dam, where the O II velocity at peak is  $3000 \text{ km s}^{-1}$  slower than that of Fe II (Quimby et al. 2018).

**Table 1**  
Excluded Regions in LC Modeling

Name	MJD (days)	Name	MJD (days)
SN 2018hpg	$< 58,385$	SN 2020onb	$< 59,030$
SN 2018lzv	$< 58,275$	SN 2020xkv	$< 59,070$
SN 2019eot	$< 58,595$	SN 2019szu	$> 59,090$
SN 2020exj	$< 58,920$		

This is an illustration that Fe<sup>+</sup> ions need lower ionization temperatures and are located at the outer layers of ejecta, thus having higher velocities, whereas the O<sup>+</sup> ions tend to be in the inner ejecta regions with lower velocities. To avoid possible biases caused by the choice of binning for the histogram distribution, we apply kernel density estimation on all the histograms in this paper (shown as the solid lines in the histograms) using a Gaussian kernel offered by the machine-learning package Scikit-learn (Pedregosa et al. 2011).

### 3.2. Light-curve Modeling

#### 3.2.1. Model Setup

One of the primary science goals in this paper is to set constraints on the power sources for the luminous optical emission seen in the SLSNe I. The open-source software MOSFiT (Guillochon et al. 2018) is used to model the LCs of 70 (out of 77) events in the gold and silver class with good phase coverage. We exclude 3 silver and all 4 bronze events with poorly sampled data before the peak. For another 7 events, we exclude the faint data obtained at either very early or late phases. The excluded regions for 7 events are listed in Table 1. For all the other events, we include all the data in the fit. The input LC data are corrected for Galactic extinction, but not the host extinction, which is a free parameter in MOSFiT. ZTF sometimes can have multiple detections in the same band on one night. The input LC data are binned into a 1 day bin, to reduce the number of input data in the MCMC fit and avoid overweighting the epochs with multiple detections. Those data points that deviate obviously from those on the same epoch will be regarded as outliers instead of real undulations in this paper.

We run the MOSFiT via Dynamic Nested Sampling (dynesty; Speagle 2020) until each run has converged under the default stopping criterion (see their documents<sup>17</sup> for details). We choose two commonly used models, i.e., the magnetar (*sln* model in MOSFiT; Kasen & Bildsten 2010; Nicholl et al. 2017b) and the CSM+Ni (*csmni* model in MOSFiT; Chatzopoulos et al. 2013; Villar et al. 2017; Jiang et al. 2020). For the CSM+Ni model, we fit both a constant density ( $s = 0$ ) and a wind-like density ( $s = 2$ ) profile. The key parameters are listed in Table A2. Each free parameter has a prior distribution defined by MOSFiT. These prior distributions can be modified for a specific data set. For example, for most of our sources, the velocities are measured from the spectra, and we set the  $V_{ej}$  prior to a flat distribution from 0.6–1.6 times the measured velocities at the peak. Following the assumption of Nicholl et al. (2017b), we use the Fe II velocity to set the prior of  $V_{ej}$ . Considering the systematic difference between Fe II and O II velocities (shown by Quimby et al. 2018; and our measurements in Section 3.1), we add a

<sup>17</sup> <https://mosfit.readthedocs.io/en/latest/fitting.html##nested-sampling>



correction of  $3000 \text{ km s}^{-1}$  when using O II velocity. By testing the Fe II and O II velocities in Quimby et al. (2018), Liu et al. (2017b), we find this range is wide enough to counteract the influence of underestimating pre-peak Fe II velocities and the velocity evolution due to the phase differences between the spectra and LC peaks. For the events without measured velocities, we use a constant velocity range of  $3000\text{--}25,000 \text{ km s}^{-1}$ , allowing MOSFiT to estimate the velocities from the LC fitting.

For the magnetar model, we set the angle between the magnetic field and the spin axis  $\theta_{\text{PB}} = \pi/2$ . The output  $B$ -field from the MOSFiT is only the perpendicular component  $B_{\perp}$ , which relates to the total magnetic field through  $B_{\text{total}} = B_{\perp} / \sin \theta$ . For the priors of the other parameters in the magnetar model, we use probability distributions similar to the ones in Nicholl et al. (2017b). For the CSM+Ni model, we use the default distributions of CSM mass and CSM shell density. We set the mass ratio of  $^{56}\text{Ni}$  to be less than 50%, the radius of the progenitor star to have a range from 0.01 to 100 au, and the opacity  $\kappa$  from 0.05 to  $0.34 \text{ g cm}^{-2}$ . Except for  $\kappa$ , the other parameters common to both the magnetar and CSM+Ni models have the same prior distributions for consistency. Another parameter—the  $\gamma$ -ray photon leakage parameter  $\kappa_{\gamma}$ —has a constant prior of  $\log_{10} \kappa_{\gamma}$  between  $(-2, +2)$ , as used in Nicholl et al. (2017a).

Finally, for each run, MOSFiT outputs a large number of possible model LCs with different weights based on *dynesty*. We use the weighted median LC as the final model LC and evaluate the error by 16% and 84% percentiles. In fitting the observed LCs of SN 2018don with the CSM+Ni model, MOSFiT converges to different outputs with the same priors for different runs. This is primarily due to the large parameter space where the convergence could be at local minimum. In this case, we ran MOSFiT several times and use the best result indicated by the smallest reduced  $\chi^2$  parameter as defined below.

### 3.2.2. Importance of Ejecta–CSM Interaction in SLSNe I

One basic question is which of these two models fits the data better. To quantify this, we use the reduced  $\chi^2$  parameter using the numbers of fitted parameters—11 and 12 for the magnetar and the CSM+Ni model respectively.

Figure 2 shows the  $\chi^2_{\text{Mag}}$  computed for the magnetar model versus the  $\chi^2$  difference between the CSM+Ni model and the magnetar model. For the CSM+Ni model, we choose either  $s = 0$  or  $s = 2$  depending on which  $\chi^2$  is smaller. The large absolute  $\chi^2$  values can be due to underestimated photometric errors and the LC undulations. According to  $\delta\chi^2 = (\chi^2_{\text{CSM}} - \chi^2_{\text{Mag}}) / [(\chi^2_{\text{CSM}} + \chi^2_{\text{Mag}})/2]$ , we find that only a small fraction of the 70 SLSN I events clearly prefer one model, with 16 events better fit by the CSM+Ni model, and 7 by the magnetar model. The majority (47/70 = 67%) of the sample can be equally well fit by both models ( $|\delta\chi^2| < 40\%$ ). This indicates that LCs alone cannot unambiguously distinguish between these two energy sources.

The 16 events favoring the CSM+Ni model have several distinct features. First, some LCs show a steep flux drop after the primary peak, e.g., SN 2018don and SN 2020afag. This steep change of LC slope generally cannot be reproduced by the magnetar model, as revealed by the poor fits (see the dashed lines) in Figure 3. However, the CSM+Ni model with a wind-like ( $s = 2$ ) or constant ( $s = 0$ ) density profile

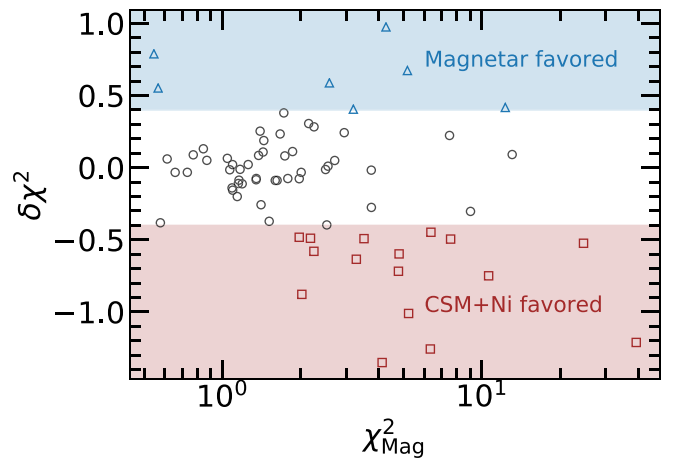


**Figure 2.** Reduced  $\chi^2$  values of the magnetar and CSM+Ni modeling. Y-axis shows the relative differences of  $\chi^2$  between these two models. The red area marks the region where the events are better fit by the CSM+Ni model, i.e.,  $\delta\chi^2 < -40\%$ , while the blue area marks the magnetar-favored region, i.e.,  $\delta\chi^2 > 40\%$ . The events in different areas are labeled with different symbols.

does much better (solid lines in Figure 3). The rapid decline has a simple physical explanation where the forward shock has run through the CSM (Chatzopoulos et al. 2012). Second, some LCs have inverted V-shaped evolution, i.e., linear rise and decline with a sharp peak, e.g., SN 2019kwt and SN 2020htd. This type of LCs can also be better fit by the CSI model, with a constant density CSM shell ( $s = 0$ ), as previously noted by Chatzopoulos et al. (2013), Wheeler et al. (2017).

The steep flux drop can also be characterized by the timescales of SLSNe I. In Paper I, we measured rise and decay timescales of the LCs for our sample and confirmed that the rise and decay timescales roughly follow a linear relation, i.e.,  $t_{\text{decay}} = 1.47 t_{\text{rise}} + 0.35$  days. In Figure 4, we plot the rise and decay timescales of our sample (similar to Figure 5 in Paper I) and highlight the SLSNe I favored by the CSM+Ni model. Most CSM-favored events are below the linear relation. They tend to have longer rise times and shorter decay times compared with those favored by the magnetar model or equally well fit by both models. Such a trend becomes more significant when including those that can be properly fit by both the CSM+Ni and magnetar models but with the former scenario being slightly favored (i.e.,  $-40\% \leq \delta\chi^2 < -20\%$ ). We applied a two-sample Kolmogorov–Smirnov test on the ratio of rise and decay times between CSM-favored events and the others. The result ( $D = 0.54$ ,  $p = 0.001$ ) shows that the CSM-favored events and the others indeed have different distributions. So we conclude that the CSM-favored SLSNe I tend to have longer rise time and faster decay time.

We infer that the minimum fraction favoring the CSM+Ni model in our sample is 23% (16/70). Half (8) of these events have smooth LCs, but clearly prefer the CSM+Ni model. Our analysis in Section 4 shows that CSI likely plays an important if not dominant role in all sources with LC undulations. In Section 4, we quantitatively identify 17 events from our sample have either weak or strong undulations. If taking into account all 17 undulating sources plus the 8 events with smooth LCs and favoring the CSM+Ni model, the fraction of CSM-powered events can be as high as 25%–44% (25/73) at a confidence level (CL) of 95% (Gehrels 1986). Such a high



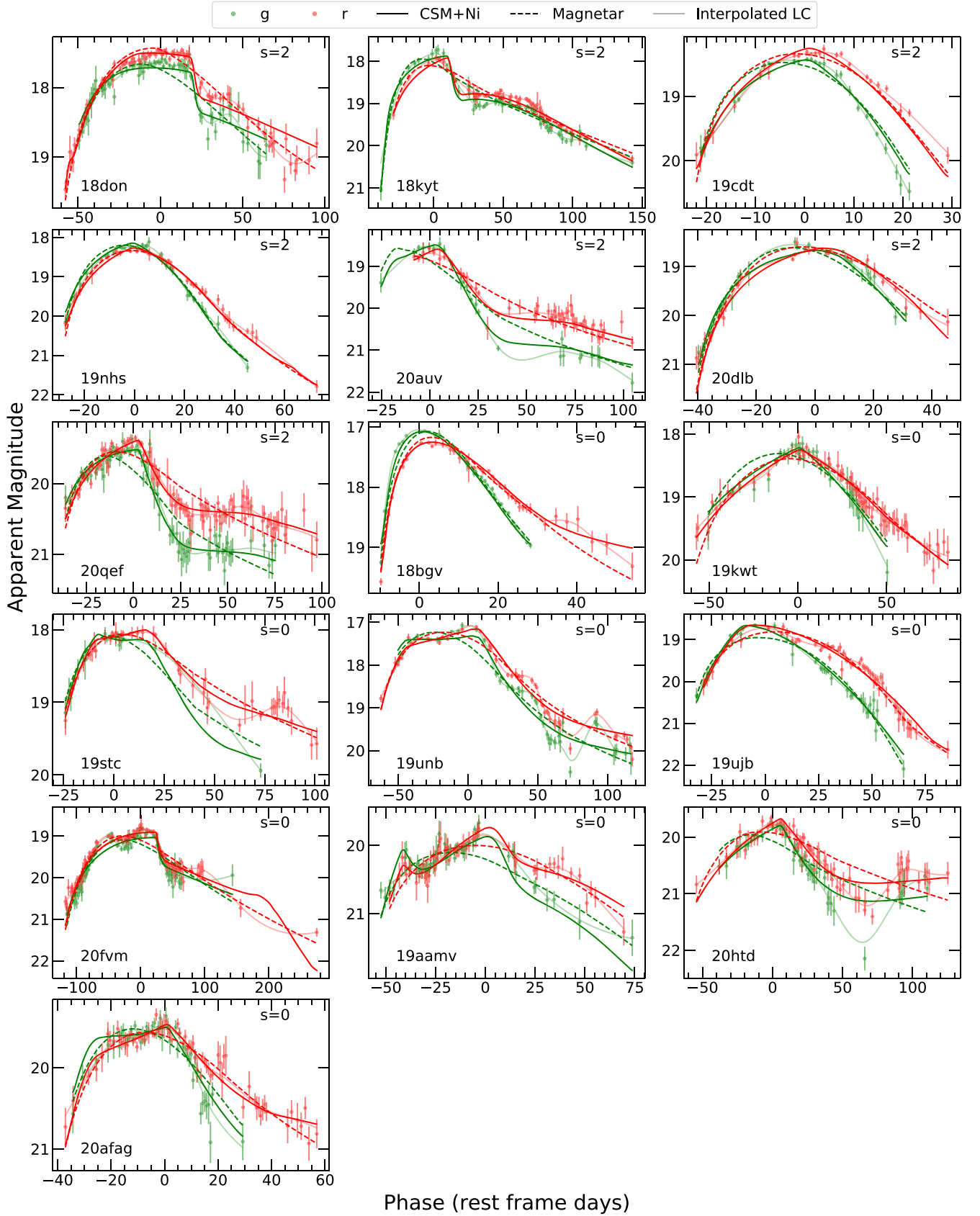


**Figure 3.** The 16 events best fit by the CSM+Ni model. CSM+Ni model, magnetar model, and GP interpolated LCs are plotted with solid lines, dashed lines, and translucent lines, respectively. The type of CSM structure, constant density ( $s = 0$ ) or wind-like ( $s = 2$ ), is labeled at the top right corner. The data in shaded region are masked out during the LC modeling.

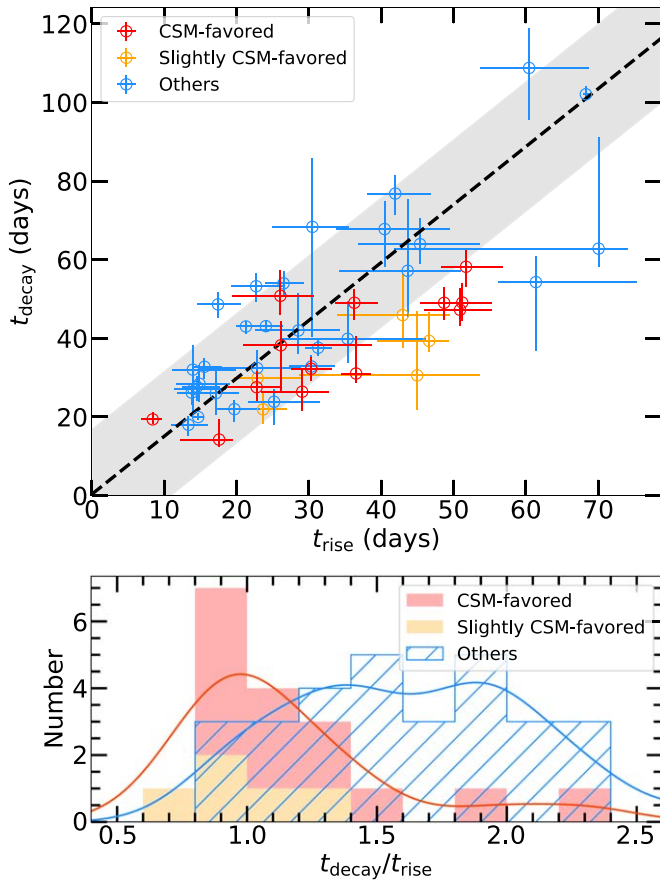


**Figure 4.** Timescales of ZTF sample (from Figure 5 in Paper I). In the upper panel, x-axes and y-axes are the rise–decay timescales. The red, yellow, blue dots represent the CSM-favored events ( $\delta\chi^2 < -40\%$ ), the ones slightly favored by the CSM+Ni model ( $-40\% \leq \delta\chi^2 < -20\%$ ), and the others, respectively. The dashed line shows the linear fit between rise and decay timescales and the corresponding  $1\sigma$  error. The lower panel shows the distribution of the  $t_{\text{decay}}/t_{\text{rise}}$  ratio. The orange solid line shows the kernel density estimation of the two CSM-favored groups, and the blue line shows that of the others.

fraction implies that H-poor (some also He-poor) CSM around SLSNe I and CSI are quite common.

### 3.2.3. Physical Parameters Derived from Model Fittings

We compare the peak luminosities and temperatures derived from MOSFiT with those from the spectral energy distribution (SED) fitting in Paper I, and find that they are largely consistent with each other, with small offsets of  $2^{+18}_{-11}\%$  and  $-1^{+9}_{-12}\%$  respectively. Figure A1 displays several relations between the derived parameters, similar to Nicholl et al. (2017b, their Figure 6).  $E_k$  is derived from  $M_{\text{ej}}$  and  $V_{\text{ph}}$ , assuming  $E_k = 0.3M_{\text{ej}}V_{\text{ph}}^2$ . This relation is valid for a homogeneous density profile, and also adopted for the CSM+Ni model. Our  $E_k$  values are thus somewhat lower than those derived by Nicholl et al. (2017b), which used  $E_k = 1/2M_{\text{ej}}V_{\text{ph}}^2$ . The overall distributions of  $P$ ,  $B_{\perp}$ ,  $M_{\text{ej}}$ , and  $E_k$  are similar to the results in Nicholl et al. (2017b), Blanchard et al. (2020), and Hsu et al. (2021). We test the correlations between these four parameters using the Spearman rank correlation coefficient. As also found by Blanchard et al. (2020), Hsu et al. (2021),  $M_{\text{ej}}$  shows a strong negative correlation ( $\rho = -0.53$ ,  $p < 10^{-5}$  in our sample) with magnetar spin period  $P$ , indicating that

SLSNe I with smaller ejecta masses require less central power with slower spinning neutron stars.

Figures 5 and 6 show the distributions of the key parameters from the magnetar model ( $P$ ,  $B_{\perp}$ ,  $M_{\text{ej}}$ , and  $E_k$ ) and the CSM+Ni model ( $M_{\text{ej}}$ ,  $M_{\text{CSM}}$ ,  $M_{\text{Ni}}$ , and  $E_k$ ). The median values and the  $1\sigma$  errors (16% and 84% percentiles) of the key parameters from the two models are listed in Table 2. The CSM+Ni model we use in MOSFiT is based on the semianalytic model from Chatzopoulos et al. (2012, 2013). However, it has been shown that the semianalytic model and hydrodynamic simulations can produce inconsistent results assuming the same CSM structure (Moriya et al. 2013; Sorokina et al. 2016). The quantitative value of the CSM parameters from the CSM+Ni model could be just an order of magnitude estimate.

Compared with the magnetar model, the  $M_{\text{ej}}$  estimates from the CSM+Ni model are significantly higher. The final mass of the progenitor star  $M_{\text{prog}}$  is estimated by summing up  $M_{\text{ej}}$  and neutron-star mass for the magnetar model, and  $M_{\text{ej}}$ ,  $M_{\text{CSM}}$  plus a typical neutron-star mass ( $1.4M_{\odot}$ , Lattimer & Prakash 2007) for the CSM+Ni model. Note that the progenitor mass calculated with this method is just a lower limit. Figure 7 shows the mass estimates for the 47 events that are equally well fit by both the magnetar and CSM+Ni models. The progenitor mass derived from the magnetar model has a median value of  $6.83^{+4.04}_{-2.45} M_{\odot}$  while it is  $17.92^{+24.11}_{-9.82} M_{\odot}$  from the CSM+Ni model.

Assuming a stellar population with low metallicity (metal fraction 10% solar, i.e.,  $1-2 \times 10^{-3}$ ), we estimate the zero-age-main-sequence (ZAMS) mass using PARSEC (Bressan et al. 2012). A ZAMS mass of  $18-35 M_{\odot}$  is needed for the magnetar model while  $30-130 M_{\odot}$  is required for the CSM+Ni model. It is not surprising that the predicted progenitor and ZAMS masses for the CSM+Ni model are much larger. This reflects the fact that the CSM+Ni model needs both larger ejecta and CSM masses in order to supply sufficient energy, as also noted previously by Chatzopoulos et al. (2013). More importantly, the high ZAMS values for the CSM+Ni model are in the regime ( $70-140 M_{\odot}$ ) where pulsational electron–positron PISN are expected to explode (PPISN; Woosley 2017). PPISN events will also experience violent episodic mass losses. This may naturally explain the presence of substantial amount of CSM. On the other hand, around half (9) of the CSM-favored events have kinetic energies higher than  $5 \times 10^{51}$  erg, which exceed the highest value for PPISN events (Woosley 2017). PISN (Kasen et al. 2011; Dessart et al. 2012), which predicts higher kinetic energies and slow-evolving LCs, could explain the three events with rise time longer than 90 days. However, for the other six events, a central engine (e.g., magnetar or black hole fallback; Kasen & Bildsten 2010; Dexter & Kasen 2013) plus CSI is likely needed to provide such a high energy.

Another parameter that can significantly impact the ejecta mass estimates is  $\kappa_{\gamma}$ , the  $\gamma$ -ray photon leakage parameter. The smaller  $\kappa_{\gamma}$  values, the faster LC decays, and as compensation, the larger ejecta masses are needed to fit the late-time LCs. The MOSFiT derived  $\log_{10} \kappa_{\gamma}$  values for the majority of our sample are  $> -1.6$ , with a small fraction (8 of 70 for the magnetar model and 2 for the CSM+Ni model) having  $-1.96 < \log_{10} \kappa_{\gamma} < -1.6$ .

Recently, Vurm & Metzger (2021) carried out 3D Monte Carlo radiative transfer calculations on SLSNe I using the magnetar model and showed that  $\log_{10} \kappa_{\gamma} = -2$  is an extremely

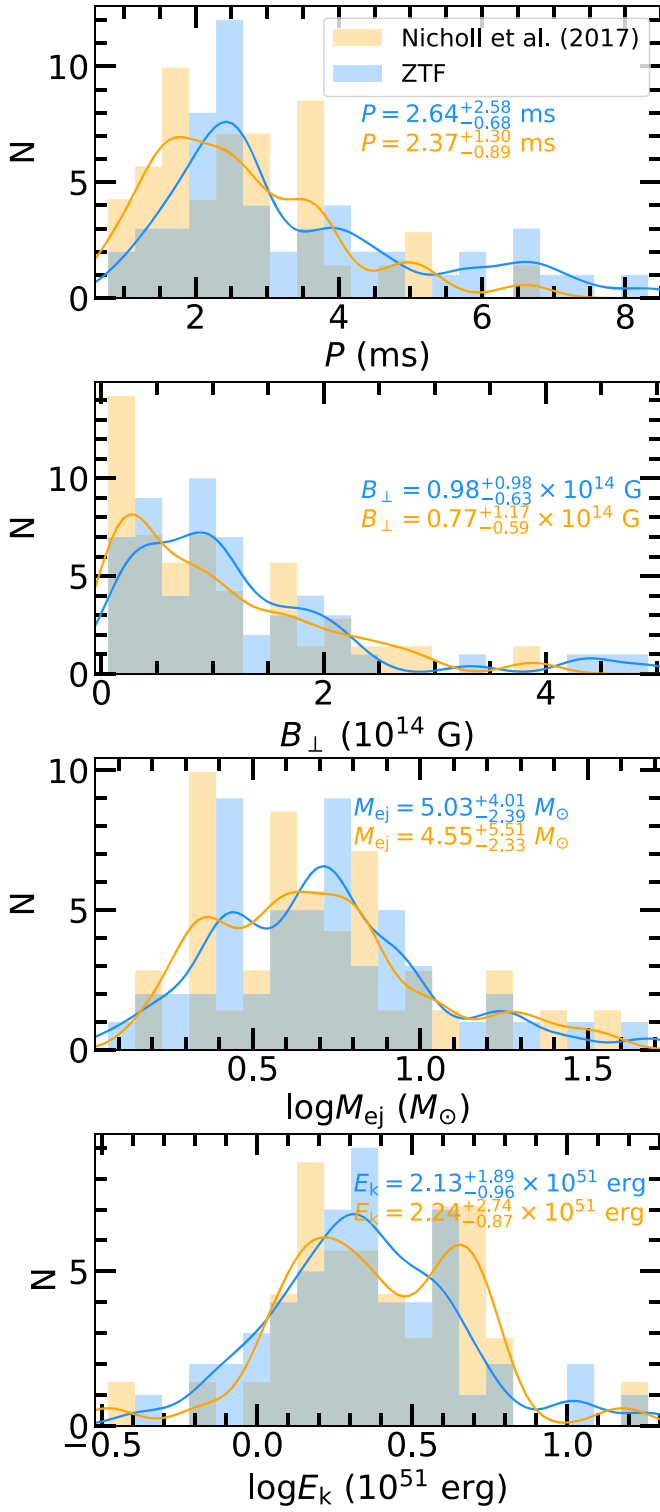


**Figure 5.** Distribution of a series of important parameters ( $P$ ,  $B_{\perp}$ ,  $M_{\text{ej}}$ ,  $E_k$ ) in the magnetar model. The blue color indicates the distribution and median value for the 54 (7+47) SLSNe I fit by the magnetar models (7 events favor the magnetar models, and 47 can be fit equally well by both the CSM+Ni and magnetar models). Those from Nicholl et al. (2017b) are shown in orange for comparison (total number is normalized to that of ZTF sample). The solid lines show the kernel density estimation of the distributions.

low value for a phase  $<300$  days (see their Figure 10). Such low  $\kappa_{\gamma}$  requires highly efficient dissipation of the magnetic field or that the spin-down luminosity decays significantly faster than the canonical dipole rate  $\propto t^{-2}$  in a

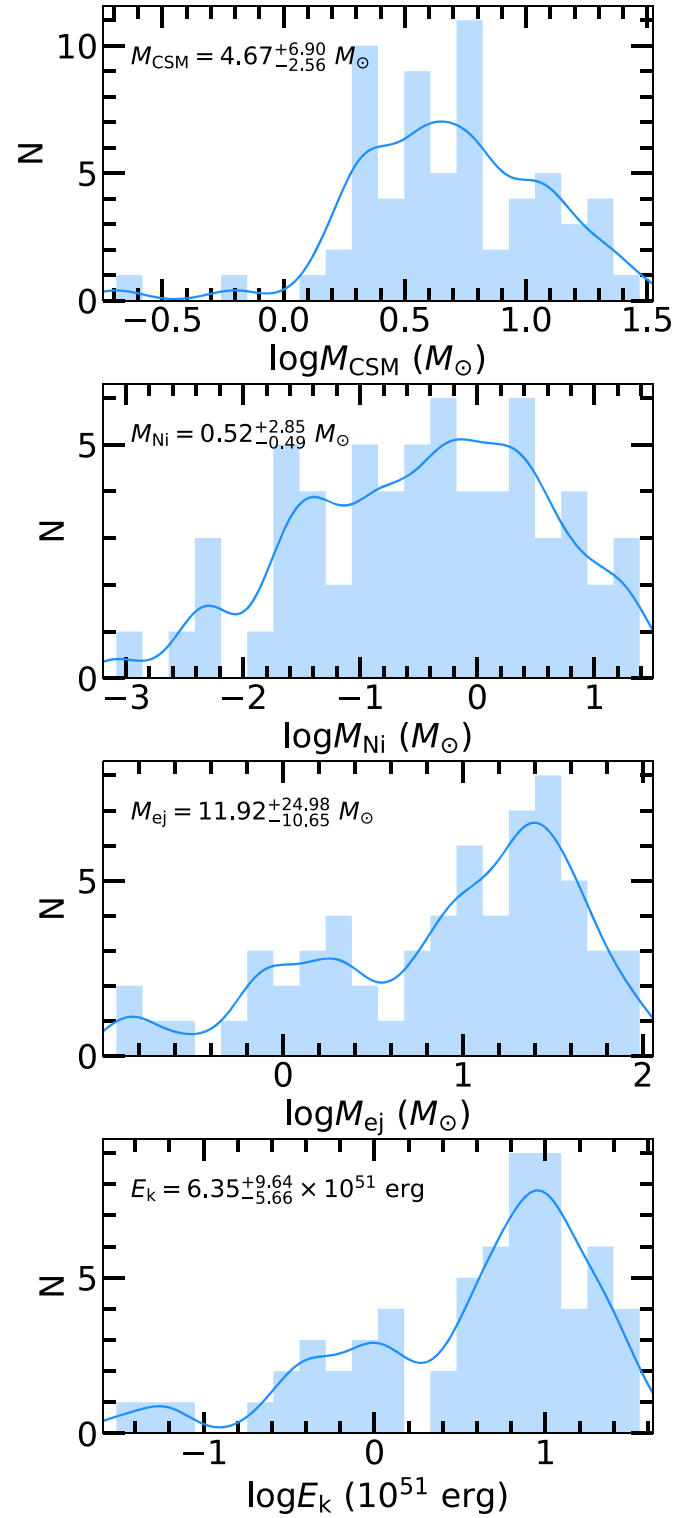


**Figure 6.** Distribution of key parameters ( $M_{\text{ej}}$ ,  $M_{\text{CSM}}$ ,  $M_{\text{Ni}}$ ,  $E_k$ ) derived for the CSM+Ni model. Here we include the 16 SLSNe I favored by the CSM+Ni models and the 47 events that can be fit equally well by both the CSM+Ni and magnetar models. The solid lines show the kernel density estimation of the distributions.

way that coincidentally mimics gamma-ray escape. We conclude that our assumed prior  $(-2, +2)$  for  $\kappa_{\gamma}$  is sufficient, and we do not need to explore a wider range of the distribution.



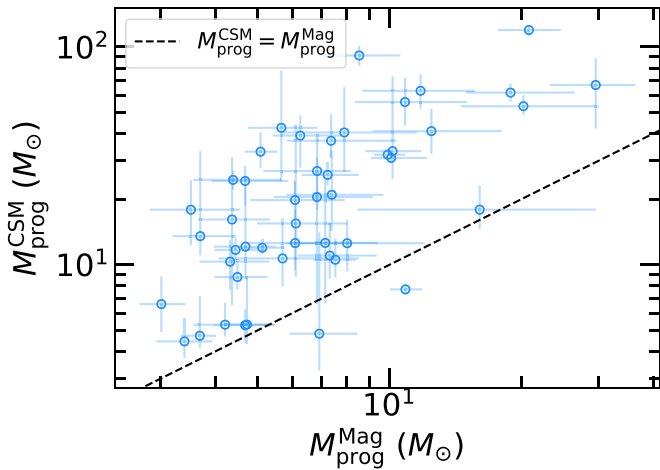


**Figure 7.** Progenitor mass  $M_{\text{prog}}$  derived from the magnetar model (x-axis) and from the CSM+Ni model (y-axis) for the 47 SLSNe I for which both models are equally good fits.

**Table 2**  
Medians of Key Modeling Parameters

Parameter	Magnetar	CSM+Ni
$P$ (ms)	$2.64^{+2.58}_{-0.68}$	...
$B_{\perp}$ ( $10^{14}$ G)	$0.98^{+0.98}_{-0.63}$	...
$M_{\text{CSM}}$ ( $M_{\odot}$ )	...	$4.67^{+6.90}_{-2.56}$
$M_{\text{Ni}}$ ( $M_{\odot}$ )	...	$0.52^{+2.85}_{-0.49}$
$M_{\text{ej}}$ ( $M_{\odot}$ )	$5.03^{+4.01}_{-2.39}$	$11.92^{+24.98}_{-10.65}$
$E_k$ ( $10^{51}$ erg)	$2.13^{+1.89}_{-0.96}$	$6.35^{+9.64}_{-5.66}$

## 4. Light-curve Morphologies

### 4.1. Early Double-peak Light Curves

Some SLSNe I have a weak bump in the early phase, e.g., SN 2006oz (Leloudas et al. 2012), LSQ14bdq (Nicholl et al. 2015a), DES14X3taz (Smith et al. 2016), and SN 2018bsz (Anderson et al. 2018). Nicholl & Smartt (2016) speculated that most SLSNe I may have such early bump features. This was shown to be incorrect by the SLSN I sample from the Dark Energy Survey (DES), which has very deep photometric limits (Angus et al. 2019). Of the 12 DES SLSNe I with pre-peak LCs, only 4 showed such a precursor bump.

We also search for early bump features in our SLSN I sample. We bin the LC data into 1 day bins and include only data with supernova remnant (SNR)  $> 3$  in our analysis. We focus on the 15 events that have very early and deep observations after the explosion. These 15 events have at least 4 epochs of pre-peak data that are 1.5 mag fainter than their main peaks. We find that only three events, SN 2019eot, SN 2019neq, and SN 2019aamt, show reliable early peak features. This corresponds to a fraction of 6%–44% (3/15, CL = 95%). This is consistent with the observed fraction (i.e., 4/12) in Angus et al. (2019). The LCs of these three SLSNe I are shown in Figure 8, together with the rest-frame  $g$ -band LCs of SN 2006oz, LSQ14bdq, and DES14X3taz. The early bumps are detected only in rest-frame  $g$  band (observed  $r$  band) in SN 2019eot and SN 2019aamt, whereas in SN 2019neq the initial peak is present in both the  $g$ - and  $r$ -band LCs (rest frame). The early bump is fit by a second-order polynomial whereas the primary peak is fit by the

Gaussian Process (GP) method. We define the width of the first peak as the time interval between the two phases when the LC is 2 mag fainter than the peak. The measured time widths and the absolute magnitudes of the first peak are listed in Table 3. The widths of the early bumps are comparable to the predictions of 10–20 days from the shock cooling models by Piro (2015).

An alternative model—magnetar shock breakout through pre-explosion ejecta (Kasen et al. 2016)—can also explain the early bumps of SLSNe I. In these models, the early bumps are more obvious if the power engine for the primary peak is inefficiently thermalized at the first 15–43 days after the explosion (Kasen et al. 2016; Liu et al. 2021). The early bumps in SN 2019neq and SN 2019aamt are shallower, which perhaps implies that their magnetar energy thermalization is relatively more efficient.

It is worth noting that among the double-peaked SLSNe I, SN 2019neq is peculiar, and has a narrow early bump width (9.07 days) and a short main peak rise time ( $\lesssim 25$  days). This makes it the fastest-evolving SLSNe I with early bumps up to date. So far most SLSNe I with early bumps are slow events (rise time  $\sim 33$ –100 days, Inserra 2019). This could be due to the observational selection bias because the fast-evolving events with narrow early bumps can be easily missed by SN surveys unless with high cadence and early sensitive detections.

### 4.2. Undulations in the Light Curves

Our large sample of SLSNe I and their LCs with excellent phase coverage provide a great opportunity to examine the LC undulation properties systematically. We perform analysis of the LCs of the 73 events in the gold and silver subclasses. All four events in the bronze class are excluded because of the sparse phase coverage of the LCs. To quantitatively identify the undulations, we compute the residual LC (RLC) by subtracting out a smooth baseline (produced by the `MOSFIT` models) from the observed LC. In our modeling and analysis, we did not manually exclude the undulating phases. The model LCs will go through undulations, and the resulting bumps and dips in the RLCs reflect how the LCs of SLSNe I deviate from the standard models. The observed data are interpolated using the GP regression. One example is shown in Figure 9, where the RLC is shown in the bottom panel including errors due to both the GP interpolation and the baseline model. In the RLC, the strength and phase of the bump–dip can be mathematically determined by their local maximum and minimum, marked as black dots in Figure 9. The maximum amplitude between the adjacent minimum and maximum, recorded as  $\Delta\text{Mag}_{\text{RLC}}^{\text{max}}$ , defines how much the LC undulates. The hatched area shows the time interval of the undulation, and the detailed properties of the LC undulations are discussed in Section 4.3.

One key element in computing the RLC is how to define the smooth baseline LC. Polynomial or GP regression fitting can produce smooth baselines, but they are also easily influenced by intrinsic bumps and dips. These two methods can in principle be applied to the rebinned LCs to smooth out the intrinsic LC variations. However, to achieve optimal results, both methods rely heavily on manual labor. They are not the best choices for our large sample. Instead, we adopt the best-fit physical model LCs to define the smooth photometric evolution, derived by running `MOSFIT` on the LCs (see Section 3 for details). SN 2018bym can be equally well ( $|\delta\chi^2| < 2\%$ ) fit by both the magnetar and CSM+Ni models, and we use the magnetar model as its baseline. The last three

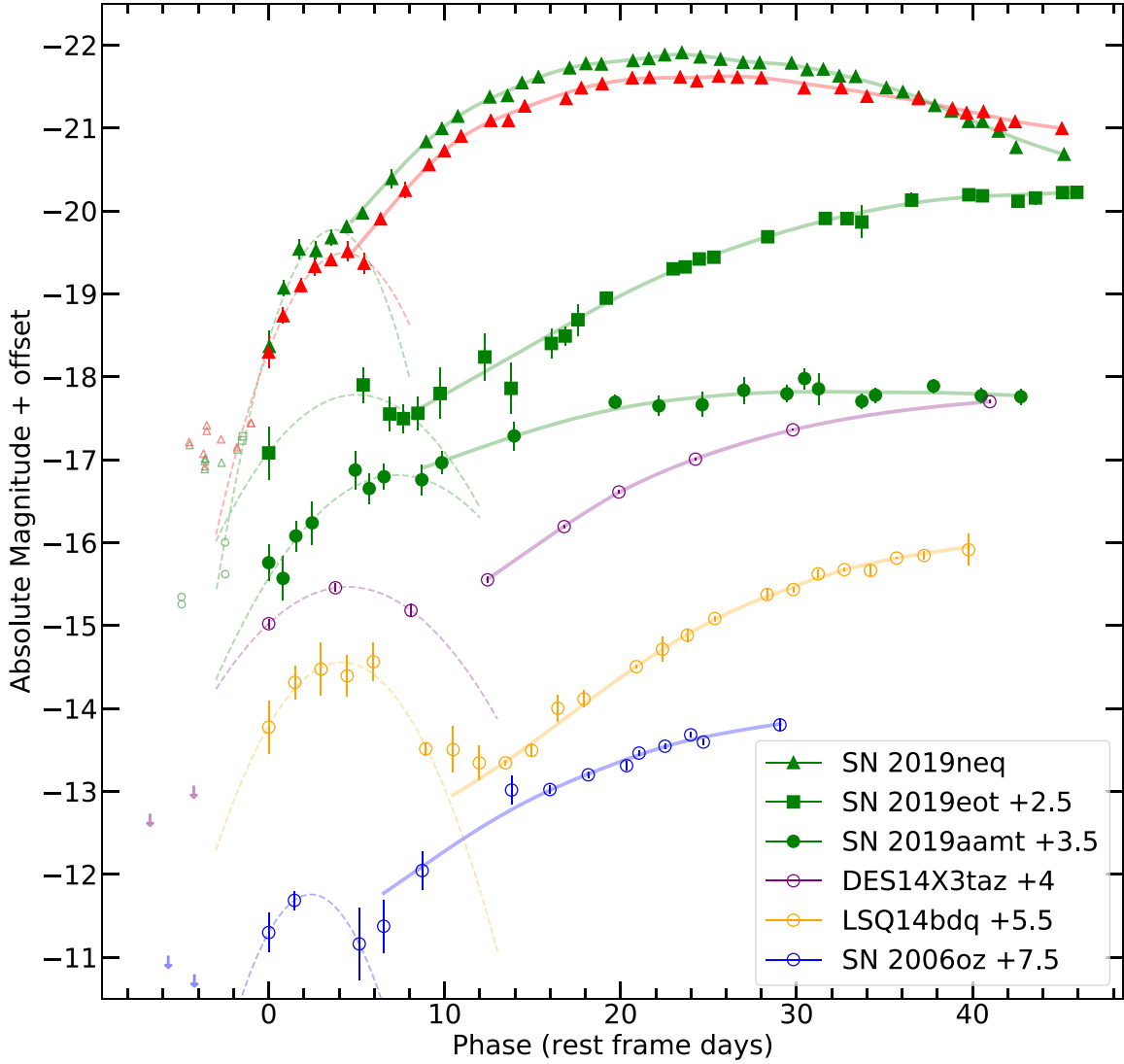


**Figure 8.** Early bump features of three ZTF SLSNe I and archival SLSNe I in rest-frame  $g$  band. The  $3\sigma$  detections of ZTF events are presented in green solid points while the upper limits are in hollow points with the same markers. SN 2019neq shows early bumps in both rest-frame  $g$  and  $r$  bands, and we highlight its  $r$ -band LC in red. Solid lines show the GP model fits of the LCs. Dashed lines show the second-order polynomial fitting applied to the early bump features.

**Table 3**  
The Properties of Early Bump Features

Name	Filter <sup>a</sup>	Width (days <sup>a</sup> )	$M_{\text{bump}}$ (mag)
SN 2019eot	$g$	17.00	-20.28
SN 2019aamt	$g$	18.56	-20.31
SN 2019neq	$g$	9.07	-19.77
SN 2019neq	$r$	11.22	-19.49
SN 2006oz	$g$	10.04	-19.26
LSQ14bdq	$g$	13.42	-20.05
DES14X3taz	$g$	19.06	-19.46

**Note.**

<sup>a</sup> Rest frame.

events (SN 2018lzw, SN 2018gkz, and SN 2019otl) are poorly sampled before peak phases, and their LCs do not show significant bump or dip features. Their baseline LCs are defined by a third-order polynomial fit. The significance of each RLC

amplitude is set by its  $\text{SNR} = |\Delta \text{Mag}_{\text{RLC}}^{\text{max}}|/1\sigma$ , where the  $1\sigma$  error includes the uncertainty from MOSFiT and GP interpolation. The significance of each undulation is determined in the same way.

The authenticity of the undulations is affected by both the photometric data and the model baselines. For the data part, to minimize the impact of occasional photometric outliers, we require the time separation between extrema to be  $>5$  days. And to avoid artificial bumps-dips produced by the interpolation in the absence of data, we require each extremum in the RLC to have at least two nearby data points within 10 days. The model part is as follows: [1] The choice of baselines (i.e., using the magnetar or CSM+Ni baseline) barely affects the identifications of undulating events, although detailed properties of undulations may change. All of the strongly undulating events and half of the weak ones identified below can pass the criteria and be identified as undulating events, no matter which model baseline is chosen. [2] In occasional cases (e.g., SN 2019lsq), the  $g$ -band model LC from the MOSFiT is significantly lower than the observed LC at the peak, while the

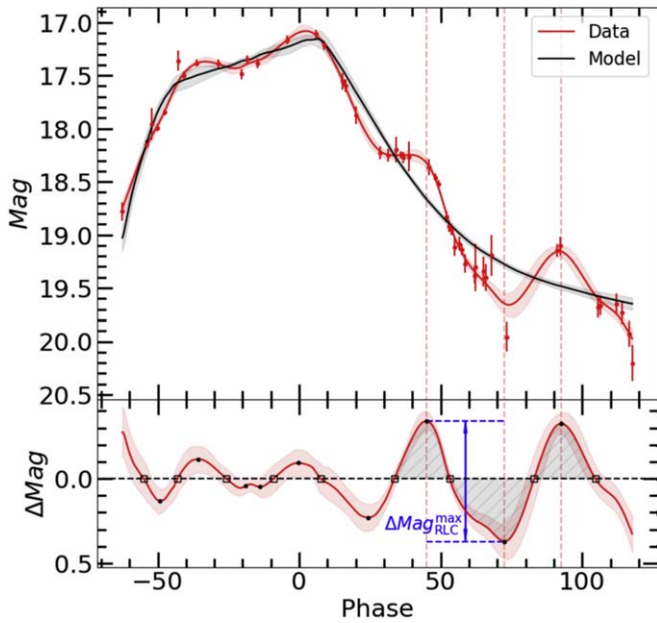


**Figure 9.** An example of the LC undulation measurements. The upper panel shows the  $r$ -band LC of SN 2019unb. The GP interpolated LC is plotted with a red line while the black line represents the LC fit with the CSM+Ni ( $s = 0$ ) model. The pink and gray shaded areas represent their  $1\sigma$  errors, respectively. The lower panel shows the residual LC (RLC) with  $1\sigma$  errors from the GP and the magnetar model. The black points represent the local extrema, and the blue vertical bar shows  $\Delta\text{Mag}_{\text{RLC}}^{\text{max}}$ , the largest magnitude change between two adjacent extrema of the RLC. The black squares mark the zero-points of the RLC. The time duration and energy of the undulations are measured from the intervals between two adjacent zero-points as shown in the hatched area. The peaks-dips of undulations are marked with the dashed vertical lines.

$r$ -band model LC fits the observed one well. It is possible that the excess detected in  $g$  band is real; however, it is also likely that the  $g$ -band luminosity at peak is underestimated by the models. This may be due to that the SED and the temperature evolution functions in MOSFiT cannot fully match the real ones. We exclude the undulations at the  $g$ -band peaks of SN 2019lsq and SN 2019neq in the following analysis, but still mark them in Figures 14 and 16 with solid points. There could be more undulations, e.g., in SN 2019cdt and SN 2019nhs, that are simply caused by the deficiency of the baseline models. However, it is difficult to distinguish whether an undulation is intrinsic or due to the local failure of the model, especially when the model LC matches the observed one in most epochs. [3] It is also possible that the smooth events (e.g., SN 2020qef) based on the CSM+Ni model are actually powered by the magnetar model plus undulations, especially considering the fact that the kinetic energies of some CSM-favored events seem too large. This would lead to an underestimation of the fraction of SLSNe I with undulations.

Figure 10 shows  $\Delta\text{Mag}_{\text{RLC}}^{\text{max}}$  versus SNR.  $\Delta\text{Mag}_{\text{RLC}}^{\text{max}}$  reflects the luminosity ratio between the bumps-dips relative to the baselines, so we also label the luminosity percentage at the top  $x$ -axis of Figure 10, where +20% and -17% correspond to  $\pm 0.2$  mag, respectively. We define a strong undulation as  $\text{SNR} \geq 3$ , and  $|\Delta\text{Mag}_{\text{RLC}}^{\text{max}}| \geq 0.2$  mag, and a weak undulation as  $\text{SNR} \geq 3$ , and  $0.1 \text{ mag} < |\Delta\text{Mag}_{\text{RLC}}^{\text{max}}| < 0.2$  mag. A total of 17 events have LC undulations with  $\text{SNR} \geq 3$ . Of these, 13 are strongly undulating sources, and 4 are weak ones. We list the strongly and weakly undulating events in Table 4. The LCs of

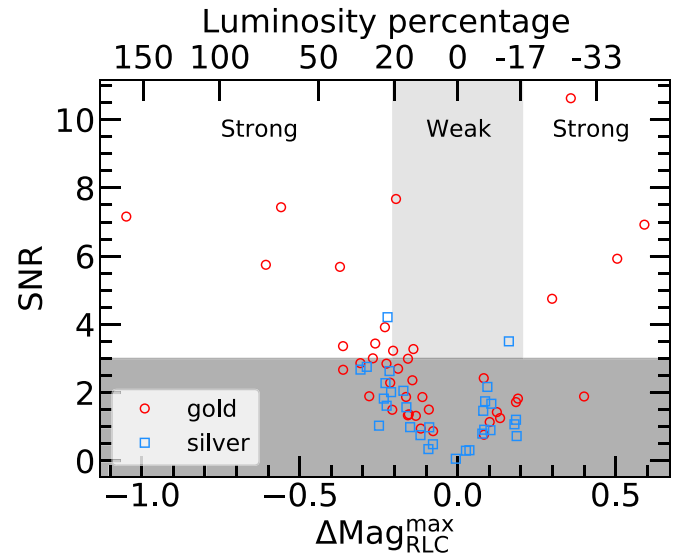


**Figure 10.** The maximum amplitude of the undulation vs. the significance.  $X$ -axis shows  $\Delta\text{Mag}_{\text{RLC}}^{\text{max}}$ , the maximum amplitude of the RLC (see Figure 9) and  $y$ -axis is the SNR, i.e., the amplitude divided by the uncertainty. The maximum amplitude is measured from either  $g$ - or  $r$ -band LCs depending on which one has the larger  $|\Delta\text{Mag}_{\text{RLC}}^{\text{max}}|$  and higher SNR. The energy percentage of the bump-dip relative to the smooth baseline LC is computed and labeled at the top. The region of  $\text{SNR} < 3$  is marked as the dark gray region, and the weak undulation amplitude region with  $|\Delta\text{Mag}_{\text{RLC}}^{\text{max}}| < 0.2$  mag is in light gray region. Events in the gold and the silver class are plotted in circles and squares, respectively.

**Table 4**  
List of 17 Undulating Events

Strong		Weak
SN 2018don	SN 2019neq	SN 2018bym
SN 2018kyt	SN 2019stc	SN 2018fcg
SN 2019kws	SN 2019unb	SN 2018lzx <sup>a</sup>
SN 2019cdt	SN 2020fvm	SN 2019eot
SN 2019hge	SN 2020htd	
SN 2019lsq	SN 2020rmv <sup>a</sup>	
SN 2019nhs		

**Note.**

<sup>a</sup> Means the event in the silver subsample.

strongly undulating sources are shown in Figures 11 and 12, and those of the 4 weakly undulating events are presented in Figure 13. It is worth noting that the CSM-favored fraction (62%, 8/13) in strongly undulating events is significantly higher than that in our whole sample (23%, 16/70). This is unlikely due to the CSM+Ni model creating more artificial undulations, because all the strongly undulating events also show strong undulations based on their magnetar baselines. Thus, this indicates that the undulations are more likely to occur in the CSM-favored event, or that the undulations make the CSM+Ni model a better fit.

Based on the above analysis, the fraction of undulating LCs is estimated to be 23% (17/73). If counting only the strongly undulating events, this fraction is 18% (13/73) while the fraction of weak undulations is 5% (4/73). However, the LCs of the silver events usually do not have complete phase coverage, and the undulation can be missed due to the lack of



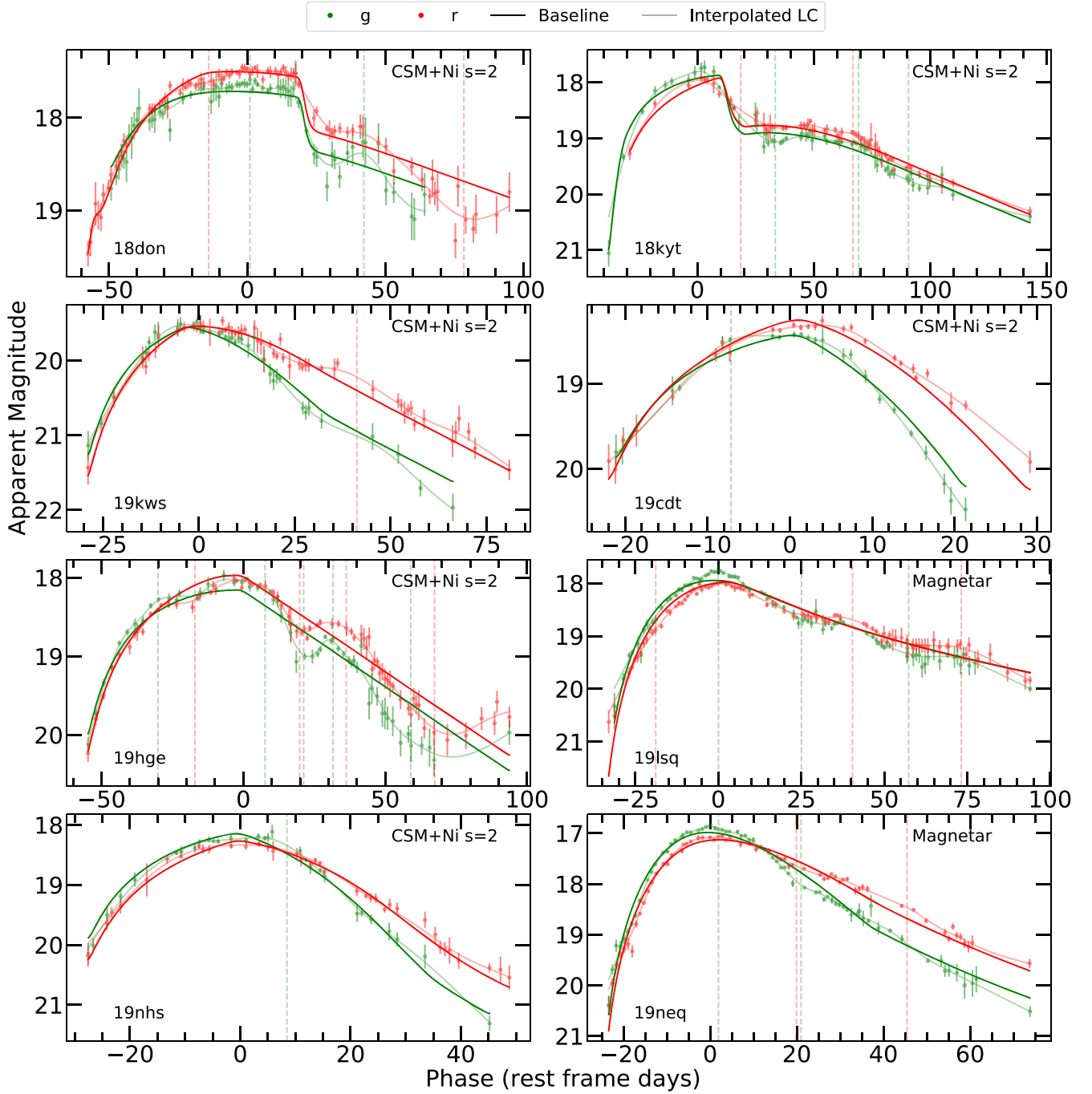


**Figure 11.** SLSN I sample with strong undulations. Baseline models and GP interpolated LCs are plotted in solid lines and translucent lines respectively. The models of the baselines are labeled at the top right corner. The peaks–dips of undulations are marked with the dashed vertical lines.

data. If we examine only the 40 events in the gold class, the fraction of undulating events is 25%–52% (15/40, CL = 95%), and the fraction of strong undulations is 18%–44% (12/40). This suggests that the LC undulations are very common in the SLSN I population. We note that sometimes it is difficult to distinguish weak undulations and observation biases, so we suggest using the fraction of the strongly undulating events in gold sample, i.e., 18%–44%. As discussed in the paragraph about the authenticity of undulations in this subsection, some undulations could be simply identified due to the deficiency of baseline models. This may apply to the undulations of SN 2019cdt and SN 2019nhs. Moreover, if removing these

two events, the fraction of undulating events will be 14%–39% (10/40, CL = 95%).

#### 4.3. Time Scales and Energetics of LC Undulations

From the RLCs, we can measure additional parameters, including phase, strength, time interval, and energetics of each undulation. In this subsection, we focus on the 13 strongly undulating SLSNe I, each of which may have multiple bumps–dips. We define the phase and the strength of each bump–dip by the time relative the peak phase and the amplitude of the RLC,  $\text{Mag}_{\text{RLC}}$ , when the RLC reaches the maximum–minimum, respectively. Counting only the significant

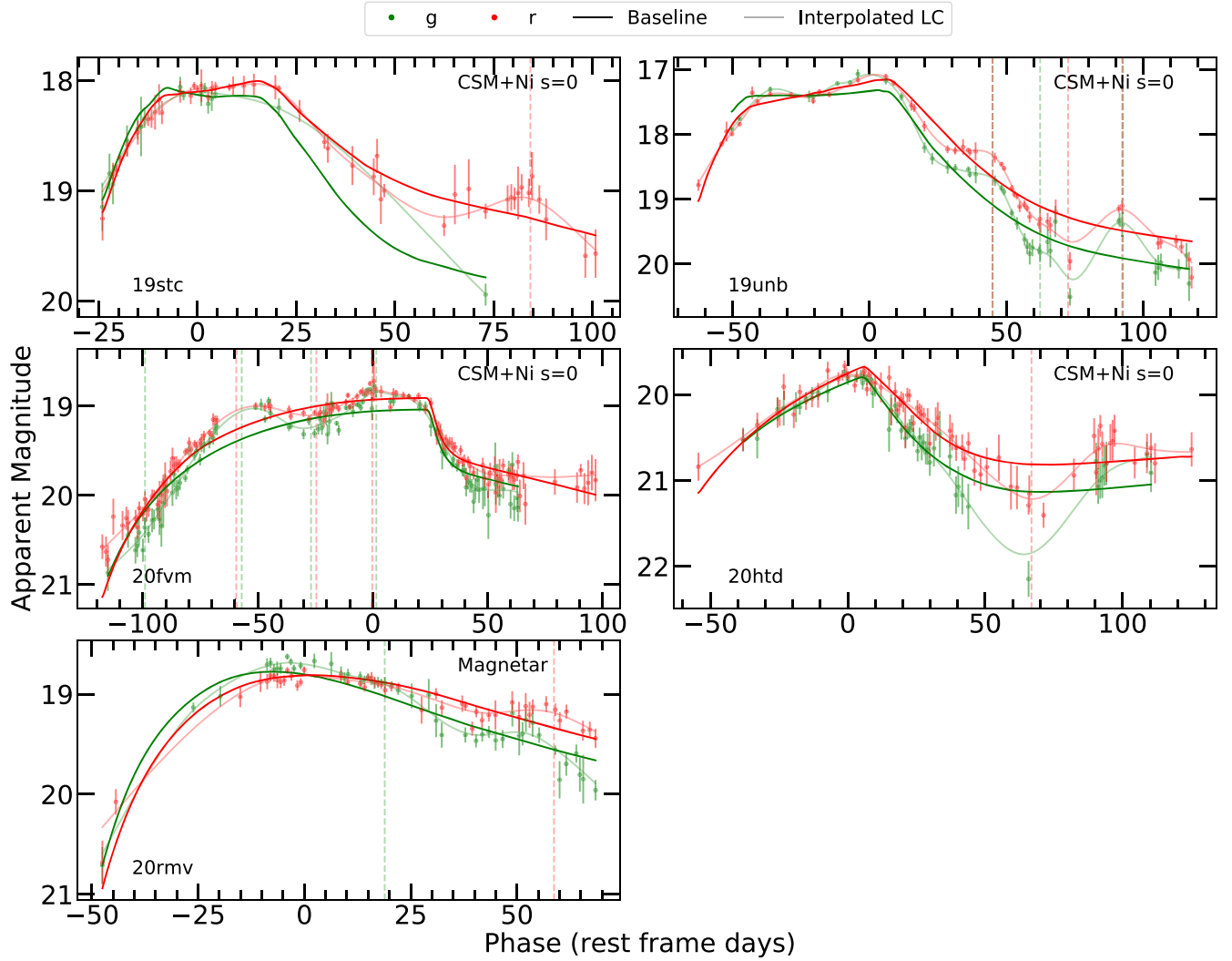


Figure 12. Similar to Figure 11.

undulations with the RLC  $\text{SNR} > 3$ ,<sup>18</sup> we identify 23 undulations in the both  $g$  and  $r$  band. This implies that, on average, each undulating LC has roughly 2 significant bumps and dips.

Figure 14 presents the phase against the strength of the significant undulations, as well as their distributions. Bumps and dips each account for around half of the undulations. 76% of the undulations appear at post-peak phases, and all the strong undulations (e.g.,  $|\text{Mag}_{\text{RLC}}| > 0.3$  mag) occur post peak. This indicates that pre-peak undulations are weaker and less common compared with post-peak ones, which is expected because the pre-peak LCs are usually much shorter than that of post-peak.

The next parameter is the time interval,  $\Delta t$ , which is defined as the time duration between two phases when their RLC values are 0 (see Figure 9). The  $\Delta t$  in strongly undulating events has a wide range from 11 to 61 days, with a median value and  $1\sigma$  error of  $28.8^{+14.4}_{-9.1}$  days. For the central engine models (magnetar or black hole fallback,

Kasen & Bildsten 2010; Dexter & Kasen 2013), the LC undulations could originate from the temporal change of the central source (see discussion in Section 5). However, any temporal variation from a central engine is smoothed by the photon diffusion in the expanding ejecta, and rapid variations would get washed out if the diffusion time is long.

Here  $\Delta t$  can be compared with  $t_{\text{diff}}^{\text{eff}}$ , the effective photon diffusion timescale, defined as

$$t_{\text{diff}}^{\text{eff}} = \left( \frac{2\kappa M_{\text{ej}}}{\beta c V_{\text{ej}}} \right)^{1/2}, \quad (1)$$

where  $\beta$  is a constant that equals 13.7, and  $\kappa$ ,  $M_{\text{ej}}$ , and  $V_{\text{ej}}$  are opacity, ejecta mass, and velocity, respectively. The instantaneous diffusion timescale,  $t_{\text{diff}}$ , can be calculated as  $(t_{\text{diff}}^{\text{eff}})^2/t$ , where  $t$  is the phase relative to the explosion date taken from the MOSFiT modeling. After the peak, the ejecta gradually becomes transparent, and the photospheric radius recedes inward. The instantaneous diffusion time of photons becomes shorter. The ratio of  $\Delta t/t_{\text{diff}}^{\text{eff}}$  or  $\Delta t/t_{\text{diff}}$  (approximately the  $\delta$  in H22) is a good indicator of whether the variable central engine scenario may drive the LC undulations. Specifically, if this ratio is less than 1, this model cannot explain the

<sup>18</sup> The undulations of SN 2019kws, SN 2019nhs, SN 2020afag, and SN 2018don (one  $g$ -band undulation at +42 days) are manually included, because their adjacent minimum and maximum each contribute to half of the  $\Delta\text{Mag}_{\text{RLC}}^{\text{max}}$ , and neither has  $\text{SNR} > 3$ .

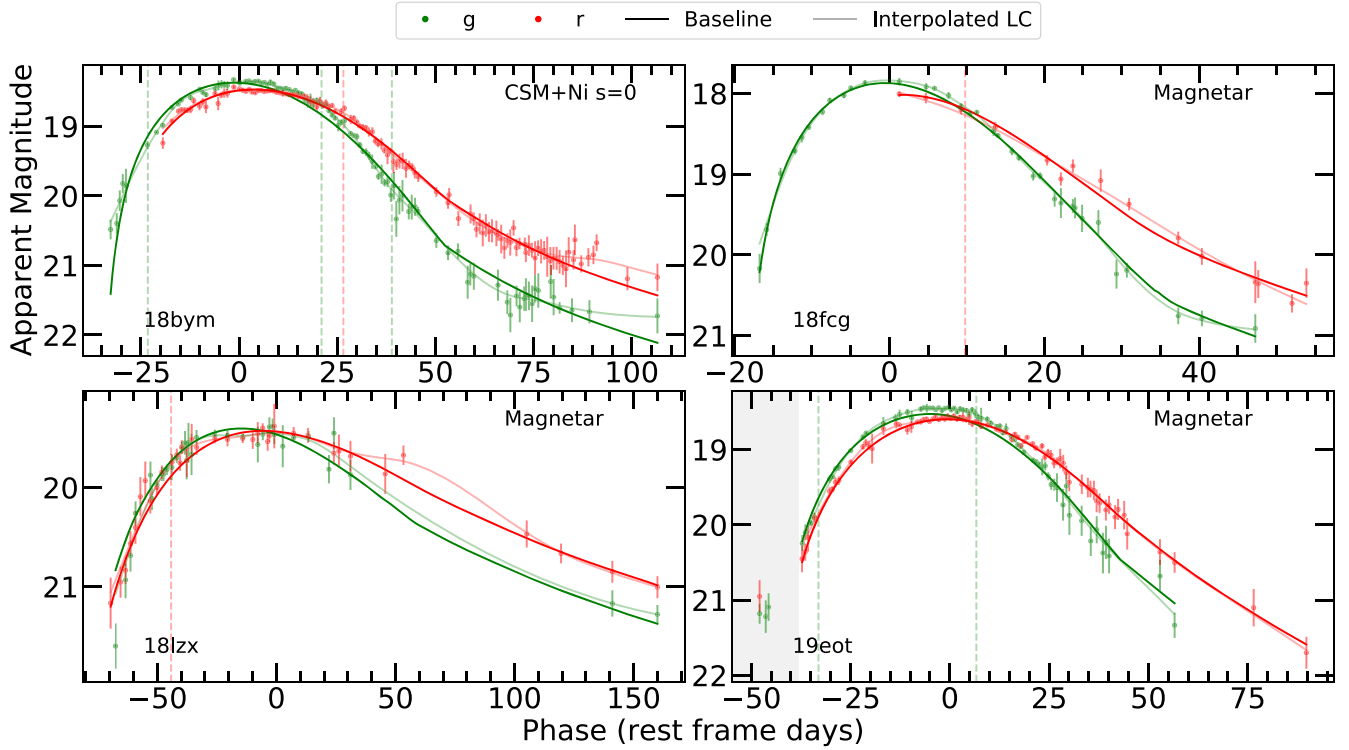


**Figure 13.** SLSN I sample with weak undulations. Similar to Figure 11. The gray shaded area marks the data excluded from the fitting.

undulations because of the smearing effect from the photon diffusion process.

Of the 13 strongly undulating events, only 5 can be fit by the magnetar model. Figure 15 displays their  $\Delta t$  versus the ratios of  $\Delta t/t_{\text{diff}}^{\text{eff}}$  and  $\Delta t/t_{\text{diff}}$ . We find that 55% (11/20) of the undulations are shorter than  $t_{\text{diff}}^{\text{eff}}$ , and 35% (7/20) are shorter than  $t_{\text{diff}}$ . 60% (3/5) and 20% (1/5) of the strongly undulating events have shorter undulations relative to either  $t_{\text{diff}}^{\text{eff}}$  or  $t_{\text{diff}}$ , respectively. Roughly half of the LC undulations (20%–60%) have time intervals shorter than the photon diffusion time-scales. This implies that emission variations of the central engine could be a viable physical explanation for about 50% of the undulations. For the other 50%, other physical processes are needed because the short timescale undulations would get smoothed out by photon diffusion.

Finally, we measure the monochromatic energy of each significant undulation,  $E_{\lambda, \text{undu}}$ , by integrating the flux differences between the LC and its baseline model (shown as the hatched area in Figure 9). We compute the ratio between  $E_{\lambda, \text{undu}}$  and the total monochromatic energy of the entire LC,  $E_{\lambda, \text{total}}$  for each undulation. Figure 16 plots the undulation energy versus the ratio. It is worth noting that most undulations appear to be quite energetic, with absolute values between  $9.1 \times 10^{48}$  to  $8.8 \times 10^{49}$  erg. However, they constitute only a small fraction of the total radiative energy, with the median energy ratio (absolute value) of  $1.7\%_{-0.7\%}^{+1.5\%}$ .

#### 4.4. Correlations

The undulation properties may have intrinsic correlations that can reveal the possible physical mechanism. We test for correlations between the phases (relative to explosion), absolute strengths, energies, time intervals of undulations, and the rise time  $t_{\text{rise}}$  (the time interval between explosion and

the LC peak). Here the explosion date is determined by MOSFIT.

H22 claimed that the phases of the post-peak bumps are moderately correlated with the LC rise times, implying that such bumps tend to happen at a certain evolutionary stage. However, observational selection effects play a significant role in their result because SLSNe I with long rising timescales are also slow declining, and undulations are preferentially detected in slow fading events. It would be difficult to observe late-time undulations in rapidly evolving events.

We carry out a simulation to quantify this observational bias. First we set  $N = 10^6$  SLSN I events, the  $t_{\text{rise}}$  of which follows the same distribution function as our whole SLSN I sample (i.e., centered at  $\sim 40$  days with an extended tail to  $\sim 140$  days). Second we let the undulations randomly occur in a time range from explosion to a maximum detectable time  $t_{\text{max}}$ . The  $t_{\text{max}}$  usually highly correlates with the  $t_{\text{rise}}$  ( $\rho = 0.60$ ,  $p < 10^{-7}$  in our sample), because  $t_{\text{max}} \approx t_{\text{rise}} + t_{\text{decay}}$ , and it has been shown that the slow-rising SLSNe I tend to decay slow by different people (Paper I; Nicholl et al. 2015b; De Cia et al. 2018). The  $t_{\text{max}}$  is thus set random in a  $\pm 67$  day wide range along the empirical relation derived from our sample,  $t_{\text{max}} \approx 1.9 t_{\text{rise}} + 35$  days. As shown in Figure 17, if only the post-peak undulations are taken into account like H22, the observational bias introduces a strong correlation ( $\rho \approx 0.67$ ,  $p \rightarrow 0$  since the number of simulated events is large) between the undulation phases and the  $t_{\text{rise}}$ . This is comparable to the value ( $\rho \approx 0.5$ ,  $p \approx 0.01$ ) measured by H22 and the one ( $\rho = 0.71$ ,  $p = 2 \times 10^{-6}$ ) measured with our real data. We further simulate samples with Gaussian or flat distributed  $t_{\text{rise}}$ , and adjust the parameters and the random range of the empirical relation in a wide range from 50% to 2 times. This correlation always exists ( $\rho = 0.53$ – $0.78$ ). Even if we calculate the correlation coefficient using both pre- and post-peak



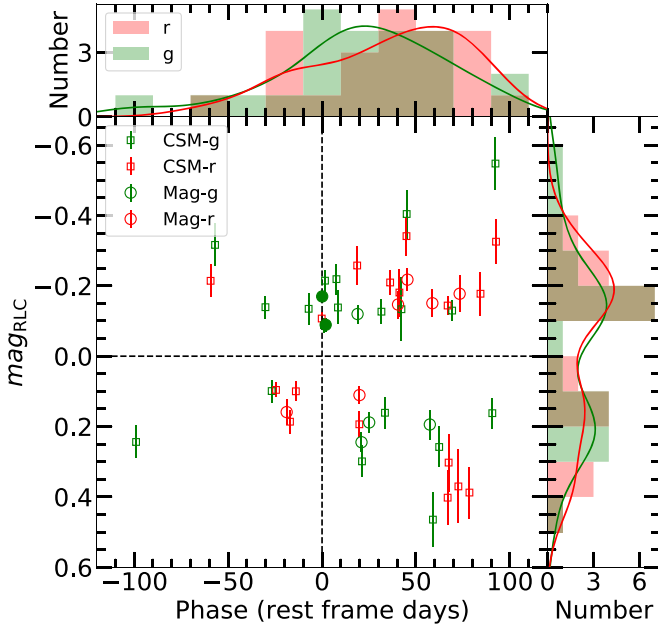


**Figure 14.** The phases vs. the strengths of undulations. The strength is defined by the magnitude of the residual LC,  $\text{Mag}_{\text{RLC}}$ , where negative value means bumps.  $g$ - and  $r$ -band undulations are plotted in green and red, respectively. The events using the CSM+Ni and magnetar baselines are marked with squares and circles, respectively. The vertical black dashed line marks the peak phase, and the horizontal one marks the boundary between bumps and dips. The histograms along  $x$ - and  $y$ -axes show the distributions of the phase and the strength, respectively. The solid lines show the kernel density estimation of the distributions. The undulations at the  $g$ -band peaks of SN 2019lsq and SN 2019neq, which could be due to the deficiency of the model, are marked with green solid points.

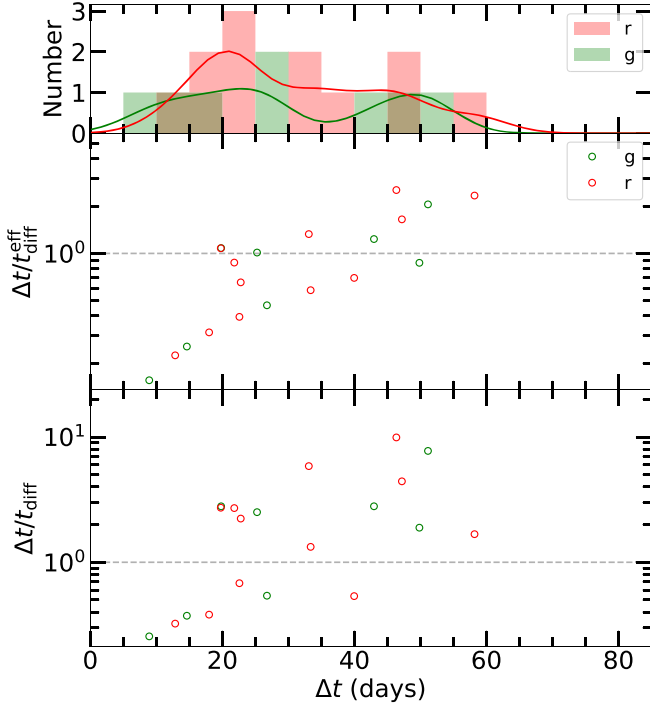


**Figure 15.** Time durations of the undulations,  $\Delta t$ , measured from the RLCs of the 5 strongly undulating events with the magnetar baselines. The top panel shows the distribution of  $\Delta t$ , and the solid lines represent the kernel density estimations. The middle panel shows the ratio of  $\Delta t$  and the effective diffusion timescale  $t_{\text{diff}}^{\text{eff}}$ . The bottom panel shows the ratio of  $\Delta t$  and the instantaneous diffusion timescale  $t_{\text{diff}}$  at the corresponding undulation phase. The dashed horizontal lines mark  $\Delta t = t_{\text{diff}}^{\text{eff}}$  and  $t_{\text{diff}}$ .

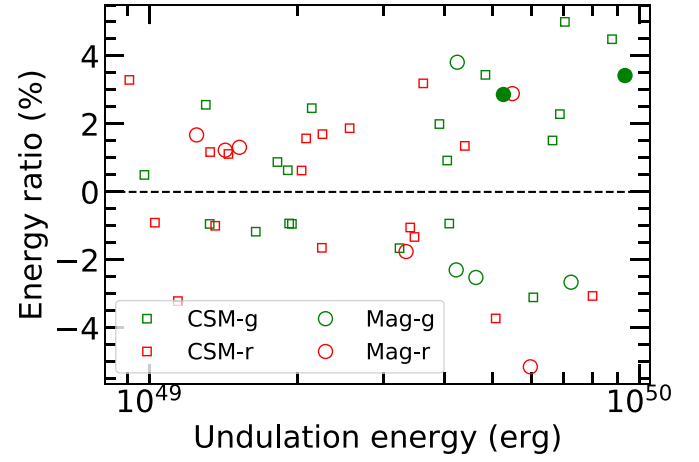


**Figure 16.** Energetics of the bumps-dips in the 13 strongly undulating events.  $X$ -axis is the integrated energy over the time interval of the undulation.  $Y$ -axis shows the ratio of undulation energy to the total radiative energy in  $g$  or  $r$  band over the entire LC. The undulations at the  $g$ -band peaks of SN 2019lsq and SN 2019neq, which could be due to the deficiency of the model, are marked with green solid points.

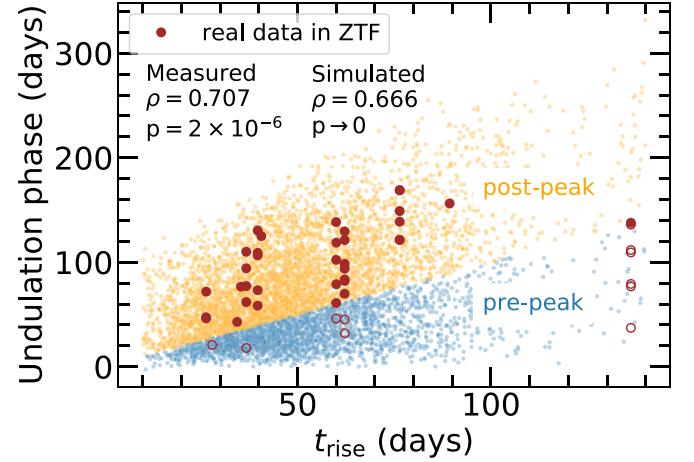


**Figure 17.** The observational selection effects on the rise times and the undulation phases (relative to explosion). Pre- and post-peak simulated undulations (1% of total) are plotted here with blue and yellow dots, respectively. The measured data from our sample is presented in brown, with open-solid dots for pre-post-peak bumps. By assuming undulations randomly occur in LCs, we find that observational effects will bring a strong correlation ( $\rho \approx 0.67$ ), which is comparable to the value ( $\rho \approx 0.5$ ) measured in H22 and the one measured in our sample ( $\rho = 0.71$ ,  $p = 2 \times 10^{-6}$ ), illustrating that such a correlation is mainly caused by an observational bias.

undulations, the measured value ( $\rho = 0.48$ ,  $p < 10^{-4}$ ) and the one caused by observational bias ( $\rho \approx 0.37$ ) are still comparable. Note that the undulations with the longest  $t_{\text{rise}}$  are from SN 2020fvm, which has two LC peaks and an unusually long rise time (136 days). No matter whether we use the shorter  $t_{\text{rise}}$  calculated using its first but fainter peak or simply delete these points, the correlation does not change. We conclude that the correlation between the undulation phase and the rise time is very likely due to observational selection effects and not a physical relation.

For other parameters, we only find weak positive correlation ( $\rho = 0.41$ ,  $p = 0.004$ ) between the phase and absolute strength as shown in Figure 18. If we exclude the specially slow-evolving event, SN 2020fvm, the correlation becomes much

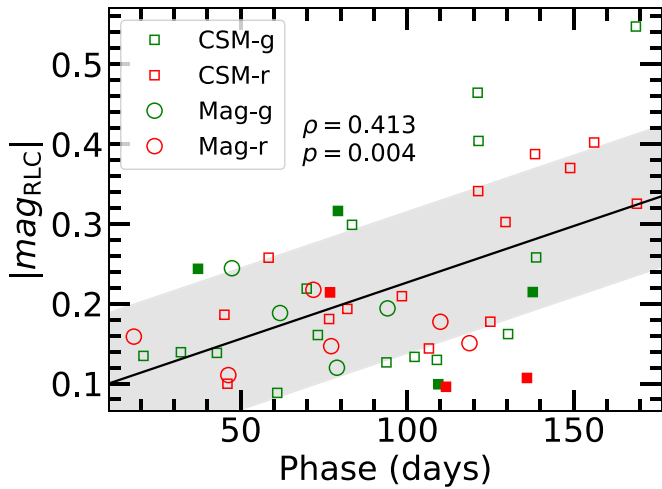


**Figure 18.** The correlation between the absolute strengths and phases of undulations. The correlation coefficient and the  $p$ -value are listed in the figure. The correlation will be much stronger if we remove the data from one unusually slow-evolving event SN 2020fvm. The data from SN 2020fvm are marked with solid symbols. The black solid line and the gray region show the result and  $1\sigma$  error of the linear fit.

stronger ( $\rho = 0.58$ ,  $p = 10^{-4}$ ). However, this correlation could also be affected by observational bias, since [1] the errors of late-time data are usually large, which makes weak undulations hard to detect; [2] the early time LCs are brighter, and the undulations require more energy to reach the same magnitude strength. No significant correlation between the phase and undulation energy also proves this. Our data are not good enough to investigate this further.

#### 4.5. Optical Colors at Bump Phases

The transient colors during the undulation phases could be an indicator of the physical processes. The observed ( $g-r$ ) colors of most of the undulations follow the general trend of the sample. However, six strongly undulating events stand out. In Figure 19, the blue lines are the observed ( $g-r$ ) color evolution tracks of six strongly undulating events. For comparison, the observed ( $g-r$ ) colors of the rest of the sample are shown in gray (see details in Paper I). Here we mark with the shaded vertical bars the period of times when the LC undulations are in excess, i.e., bump phases. These are quantitatively defined by the time intervals between the minima in the RLCs. From Figure 19, we note that, during the bump phases, the observed ( $g-r$ ) colors are significantly bluer than that of the comparison sources. In particular, three events, SN 2018don, SN 2019hge, and SN 2020rmv, show much bluer colors when their LCs are varying, and turn redder again after or at the end of the bumps. The other three events, SN 2018kyt, SN 2019lsq, and SN 2019unb, are found to show much bluer and more stable colors than the general trend seen at late times ( $>+40$  days). This result suggests that the CSM could be an important energy source, and can naturally explain both the blue colors and the strong secondary peaks at late times for these six events. The duration of the blue color phase may be affected by the thickness of the CSM. However, magnetar heating cannot be completely ruled out as different magnetar deposition profiles could also impact the color evolution at late times (Dessart 2019).

#### 4.6. LC Undulations in Helium-rich SLSNe Ib

Yan et al. (2020) reported six He-rich SLSN Ib events from the ZTF Phase I SLSN I sample. One additional event, SN 2020qef, was thereafter spectroscopically classified as an SLSN Ib by Terreran et al. (2020). Of these seven He-rich SLSNe Ib, five events, namely SN 2018kyt, SN 2019kws, SN 2019hge, SN 2019unb, and SN 2020qef, have gold LCs. Of these five SLSNe Ib, four<sup>19</sup> have strong undulations, three<sup>20</sup> show much bluer color during their bump phases, and three<sup>21</sup> strongly prefer the CSM+Ni model over the magnetar model, as shown in Figures 11, 19, and 3. All the five well-sampled He-rich SLSNe Ib either have strongly undulating LCs or the LCs are much better fit by the CSM+Ni model. This small sample appears to have a much higher undulation fraction and a higher fraction of CSM+Ni-powered LCs than those of the full sample.

These results suggest that CSM are present in He-rich SLSNe Ib and leave significant imprints on their LCs. This is consistent with a scenario proposed in Yan et al. (2020), where the progenitors of SLSNe Ib have lost most of their hydrogen envelopes but have not had enough time to also lose all of their helium layers. Because of the short time interval between the mass loss and the SN explosion, it is likely that CSM are present near the progenitor stars. This scenario can naturally explain many of the observed characteristics of SLSNe Ib, including He-rich spectra, LC undulations, and blue colors during the bumps.

As for the remaining two of the seven SLSNe Ib, SN 2019obk and SN 2019gam, both have poorly sampled LCs. The absence of undulations in their LCs could simply be due to lack of data.

### 5. Discussion

We modeled and analyzed the LCs of 70 gold and silver SLSN I events presented in Paper I. Based on two commonly used SLSN models, the magnetar model and the CSM+Ni model, we explore the properties and possible mechanisms that drive LC undulations.

#### 5.1. What Drives LC Undulations among SLSNe I?

One major finding is that LC undulations are common, about 18%–44% (12/40) of the SLSNe I show such features. This fraction should be a lower limit as we count only undulations with strength  $>0.2$  mag and  $\text{SNR} > 3$  in gold sample, and some events are not well sampled at late times. The undulation fraction for SLSNe I is therefore quite high, and likely also higher than that of SNe Ic (Lyman et al. 2016; Prentice et al. 2016), although the actual undulation fraction for SNe Ic has not been measured and requires future work. For comparison, the undulation fraction for SNe IIn appears to be quite low, only  $1.4^{+14.6}_{-1.0}\%$  from a study of 42 events from Palomar Transient Factory (Nyholm et al. 2020). This result has large uncertainties, and is therefore worth further validation with better LCs from ZTF.

The important question is what physical processes are driving the observed LC variations. There are two main possibilities. First, in the central engine scenario, the power

<sup>19</sup> SN 2018kyt, SN 2019kws, SN 2019hge, and SN 2019unb.

<sup>20</sup> SN 2018kyt, SN 2019hge, and SN 2019unb.

<sup>21</sup> SN 2018kyt, SN 2019unb, and SN 2020qef.

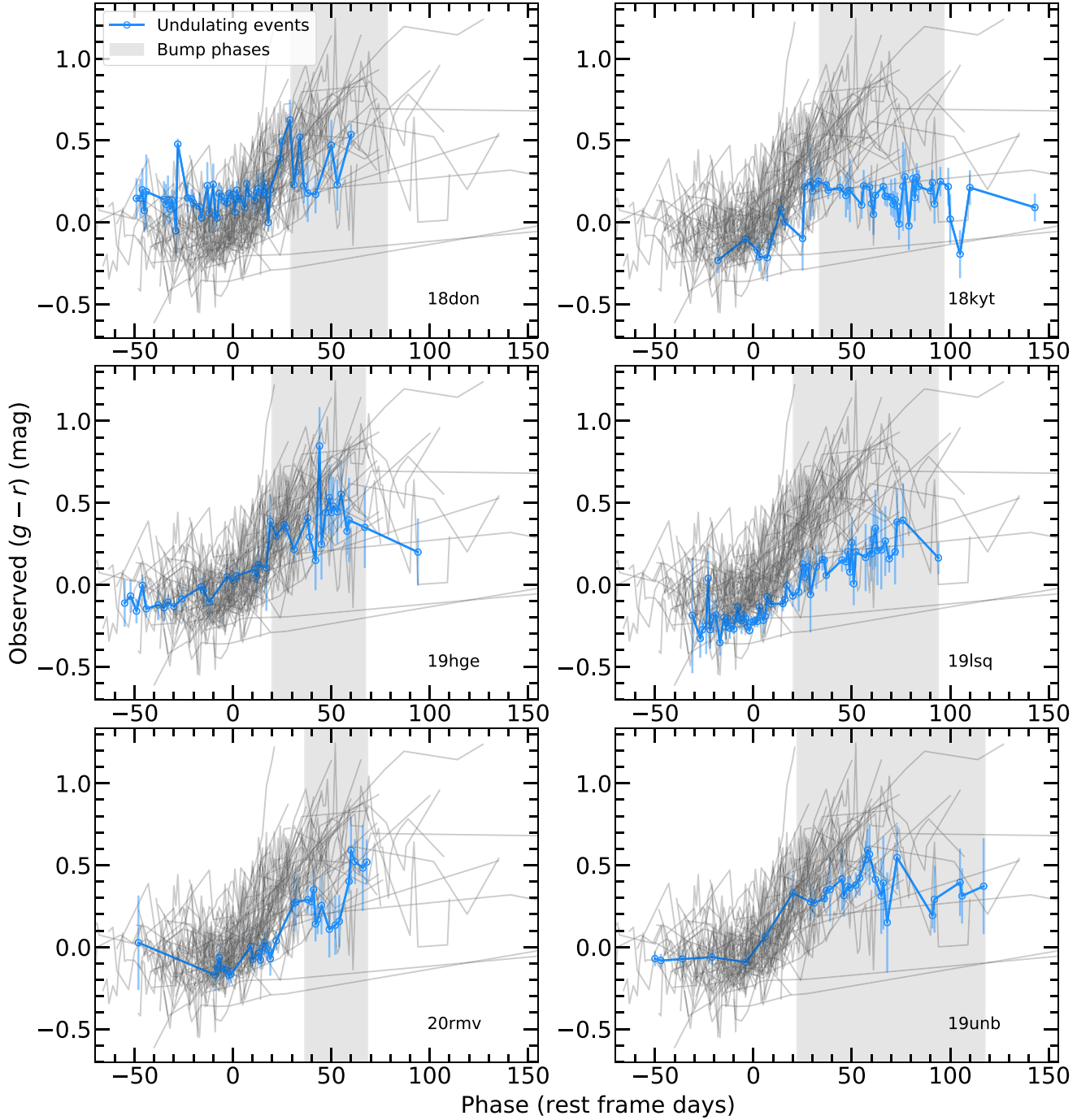


**Figure 19.** The observed  $(g - r)$  colors as a function of rest-frame days relative to the peak phases. The blue tracks in the six panels are for the 6 strongly undulating events, overlaid on top of the color tracks of the full sample (gray lines). The bump phases are marked by the shaded vertical bars. All 6 panels show that the observed  $g - r$  colors turn bluer during the bump phases.

output of the central source—either a magnetar or black hole fall-back accretion—may have a temporal variation. This intrinsic variation will be modulated (or smoothed) by photon diffusion in the ejecta. At a given phase, the variations shorter than the photon diffusion timescales will be smoothed out and not observable at that phase. Figure 15 in Section 4.3 compares the undulation and photon diffusion timescales, illustrating that the central engine temporal variations could be a viable physical explanation for only 50% of the undulations. For the other 50%, which have shorter timescale undulations, different mechanisms are likely at work.

In the variable central engine scenario, as SNe evolve, the ejecta gradually becomes transparent. This implies that the LC undulations should be stronger and more easily observed at later times. Indeed, we find 76% of undulations and several of the strongest ones all occur post peak (Section 4.3). The variable central engine scenario could be supported by the observed weak correlation between the phase and absolute strength of undulations, discussed in Section 4.4.

It is also possible that the central energy output is constant, but the ejecta opacity may undergo temporal changes, which in turn causes the variations in photospheric emission. This idea



was proposed to explain the LC undulation in the luminous transient ASASSN-15lh (Margutti et al. 2017). If a central energy source can increase the ionization of the ejecta, this can lead to higher optical opacity due to electron scattering. Furthermore, the UV opacity, dominated by metal line transitions, can decrease as the metal ions have fewer bound-bound transitions, leading to less opacity and higher UV emission. This may be the explanation for the extraordinarily UV bright, slowly evolving SLSN I SN 2019szu (see Paper I). In addition, when ejecta temperatures cool down, the recombination of ions can lead to the reduction of optical opacity. If this opacity decrease occurs quickly, it can manifest itself as an LC undulation. Another important point about the magnetar-driven model is that our current understanding is still limited, and more detailed 3D hydrodynamic simulations are beginning to find interesting results, such as strong instabilities and mixing in a magnetar-powered SN with CSM (Chen et al. 2020).

The second mechanism is ejecta–CSI. This process could be at work for at least  $\sim 50\%$  of the SLSN I undulations, and is further supported by the conclusion in Section 4.2 that the undulations are more likely to occur in the CSM-favored events. CSI is an effective means to convert mechanical energy into thermal emission, and the CSM could have a variety of geometric and density distributions, e.g., shells or clumps. Vreeswijk et al. (2017), Liu et al. (2017a), and Li et al. (2020) have applied the CSI model to explain the undulations observed in several SLSNe I. The bluer ( $g - r$ ) colors during the bump phases observed among some of our SLSNe I provide evidence supporting the CSM model (see Figure 19). The simplistic picture is that the CSI can heat the ejecta and lead to both bluer colors and excess emission.

The LC shape under the CSI mechanism is highly dependent on the density profile of the CSM. The events with multiple peaks could have multiple CSM shells or clumpy CSM structures. One possible explanation is that the progenitor undergoes violent episodic mass losses (e.g., PPISN). The other is that the SLSN I progenitor not only has an extended CSM due to significant mass loss prior to the explosion but also has a binary companion that sweeps up and enhances the CSM density while orbiting the progenitor. This idea was proposed for the radio LC of SN 2001ig by Ryder et al. (2004).

Shock breakout has also been proposed to explain SLSN I LC bumps at very early phases (so-called double-peaked LCs). The energy source could be either magnetar–black hole (Kasen et al. 2016) or CSI (Moriya & Maeda 2012; Piro 2015). Some of the basic ideas may be viable for explaining the LC undulations at late times, such as changing of ionization states thus opacities. However, it is not clear how these models can work for undulations at post-peak phases. More quantitative modeling is needed.

Besides these major models, there are other possible scenarios. For example, Kaplan & Soker (2020) suggests that the undulating LC of SN 2018don (Lunnan et al. 2020) is the geometric effect of observing a different amount of emitting area from the two expanding photospheres of fast (polar) and slow (equatorial) outflows (or jets). The Kaplan & Soker (2020) study is based on the results from Quataert et al. (2019), which finds that the outer convection zones in yellow and red supergiants can generate enough angular momentum to form an accretion disk around the black hole. This model also predicts that these accretion flows could be highly time variable.

In our analysis, about half of the undulations are dips. Dips can actually occur in the LCs when the magnetar power or the CSM density goes down, or the opacity increases (Moriya & Maeda 2012). But identifying bumps–dips depends highly on the choice of baselines, which can be ambiguous in many cases. The bumps–dips in this work reflect more on how the observed LCs deviate from the standard models, and cannot be clearly identified unless more accurate modeling is applied.

### 5.2. Prevalence of H-poor CSM in SLSNe I

Of the 70 LCs, 16 have distinct features that are much better modeled by CSI with an assumed density profile (wind or constant). The fraction of SLSNe I with H-poor CSM is between 25% and 44%, if we include events with undulations and smooth LCs preferentially fit by the CSI models.

This result has several implications for our understanding of the nature of SLSNe I. First, if CSI plays an important role in driving undulations, such a high fraction implies that, at the time of SN explosion, H-poor CSM is likely present for a large fraction of SLSNe I. This is the first time we have quantified how important CSI is for SLSNe I using a carefully selected, large sample. Previously, many studies have preferred magnetar models for the SLSN I population (Inserra et al. 2013; Nicholl et al. 2017b). One reason is its simplicity. Another indirect reason is lack of observational signatures of CSI.

The presence of H-poor CSM around SLSNe I also implies that the massive progenitor stars have not had enough time to completely disperse all of the outer envelopes before the core collapse happened. A fraction of these stars will have lost almost all their H-envelope, but their He-rich outer layers are still present before the SN explosion. These events will appear as He-rich SLSNe Ib (Yan et al. 2020). This also naturally explains why most of the SLSNe Ib have undulating LCs, which are better fit by the CSM+Ni model.

Furthermore, if the LC undulations could be explained by ejecta running into discrete CSM shells, this would imply that the progenitor mass loss is violent enough to eject large amounts of material. The CSM shell radius when the interaction occurs can be estimated by

$$R \approx V_{\text{ej}} t \quad (2)$$

where  $V_{\text{ej}}$  is the ejecta velocity output from MOSFiT, and  $t$  is the phase of the undulation. For the strongly undulating events in our sample, the radii vary from  $1.3 \times 10^{15}$  to  $1.3 \times 10^{16}$  cm with a median value of  $5.4 \times 10^{15}$  cm. Assuming a stellar wind velocity of  $10^2$ – $10^3$  km s $^{-1}$ , the CSM should be ejected several months to several decades before explosion.

### 5.3. Comparison with H22

Independent of our work, H22 recently analyzed the bumps in the post-peak LCs using a sample of 34 published SLSNe I, which have LC phase coverage out to +100 days post-peak. Eight events<sup>22</sup> are included in both their work and ours. Compared with H22, the greatest advantage of our sample is that our data is mainly from one single survey (ZTF), which is less affected by the systematic offsets and target selection from different telescopes. On the other hand, around half of our

<sup>22</sup> SN 2018bym, SN 2018fcg, SN 2018kty, SN 2019hge, SN 2019lsq, SN 2019neq, SN 2019ujb, and SN 2019unb.

sample is not sampled up to +100 days post-peak, and some undulations at such late phases will be missed in our results.

Both works use the magnetar model implemented in MOSFiT and analyze LC undulations in the RLCs by subtracting the modeling LCs from the observed ones. We additionally fit the CSM+Ni model and choose the better one as our baselines. H22 visually identified the bumps in LCs and masked the data during the bumps when modeling the baselines. To avoid human intervention in the selection of the undulating area, we keep all observed data in most events. We identify undulations by certain criteria of  $\text{SNR} > 3$ , and  $|\Delta \text{Mag}_{\text{RLCI}}^{\text{max}}| > 0.2 \text{ mag}$ .

Our conclusion for undulation fraction in SLSNe I is 18%–44% (12/40), which is based on strongly undulating events in the gold sample. This result seems slightly lower than the definite bump fraction of 44% (15/34) measured by H22, but consistent within  $1\sigma$ . The difference could be due to various reasons, including the following: [1] The baseline models and the model priors are different. Using the magnetar baseline may erroneously create undulations in the CSM-favored events while we could have also missed the undulations when using the CSM+Ni model in the magnetar-driven events. [2] Undulations are identified via certain criteria in this work but via visual inspection in H22. [3] Some events in this work are not well sampled at late time, and thus late-time undulations can be missed. Among the eight events that are common in both works, the identification of four events<sup>23</sup> is the same, while the rest (four events<sup>24</sup>) are different. More accurate modeling is needed for them. But in general, both works illustrate that LC undulations are common in SLSNe I.

H22 claimed that the phases of the bumps are moderately correlated with the LC rise times. We prove that such correlation is likely to be nonphysical, and is actually the result of observational selection effects. The energy source of LC undulations is still uncertain in both works, which requires more accurate models for SLSNe I.

## 6. Summary

The three major results from our analysis are as follows.

1. LC undulations appear to be common, with 18%–44% of the gold sample showing significant departures from their smooth baseline LCs. Most of the undulations (i.e.,  $\sim 76\%$ ) occur at post-peak phases. The energies within the undulations vary from  $9.1 \times 10^{48}$  to  $8.8 \times 10^{49}$  erg, usually  $< 5\%$  of the integrated radiative energy. The undulation time intervals and their observed  $(g-r)$  colors suggest that both the CSI and the central engine with temporal variation are possible driving mechanisms. But the central engine variation can only explain about half of the undulations while the CSI can potentially work for all undulating events. We also find that the CSM-favored fraction (62%, 8/13) in strongly undulating events is significantly higher than that in our whole sample (23%, 16/70), which implies the undulations tend to occur in the CSM-favored events.
2. Our careful LC modeling finds that the majority of the sample (47/70 = 67%) can be equally well fit by both the magnetar and CSM+Ni models. This implies that LCs alone cannot unambiguously identify the power

mechanism for SLSNe I. The large number of parameters in both of these models renders some degeneracy that cannot be broken by the LC data alone. However, a small fraction ( $16/70 = 23\%$ ) of LCs with specific features, such as inverted V-shape, steep LC decay or the features of long rise and fast post-peak decay, is clearly much better fit by the CSM+Ni model with either wind or constant density profiles. Only 7 out of 70 LCs prefer the magnetar model.

3. If LC undulations are indicators of CSI, our analysis and LC model fitting suggest that H-poor CSM is present in at least 25%–44% of the SLSN I events. If the LCs with multiple undulations are interpreted as ejecta running into several CSM shells, this would imply that their massive progenitors experience violent, episodic mass-loss events prior to the SN explosion. One such mechanism is PPISN, occurring in low-metallicity stars with ZAMS masses  $> 70 M_{\odot}$  (Woosley 2017).

We also summarize below additional statistical measurements from our sample.

1. The fraction of SLSNe I with early double-peak LCs is small, about 6%–44% (3/15) measured from a subset of LCs with early time data. This result is consistent with that of Angus et al. (2019) based on much deeper DES data. While this feature has previously been observed only in slow-evolving events, we observe a double-peak LC in a fast-evolving SLSN I, SN 2019neq.
2. For the 54 events that can be fit by the magnetar model, we find  $P = 2.64^{+2.58}_{-0.68}$  ms,  $B_{\perp} = 0.98^{+0.98}_{-0.63} \times 10^{14}$  G,  $M_{\text{ej}} = 5.03^{+4.01}_{-2.39} M_{\odot}$ , and  $E_k = 2.13^{+1.89}_{-0.96} \times 10^{51}$  erg. We confirm the anticorrelation between  $M_{\text{ej}}$  and  $P$  found previously (Nicholl et al. 2017b; Blanchard et al. 2020; Hsu et al. 2021).
3. For the 47 events that can be fit equally well by both models, the final progenitor masses span over  $6.83^{+4.04}_{-2.45} M_{\odot}$  and  $17.92^{+24.11}_{-9.82} M_{\odot}$ , estimated from the magnetar model and the CSM+Ni model respectively. The CSM+Ni model thus requires a much more massive progenitor.

In conclusion, our analysis of a large number of SLSN I LCs has revealed and confirmed several important observational properties, which only become obvious after the high cadence and well-sampled ZTF LCs are available. Both LC shapes and the high fraction of undulations show clear indications that CSM may be present near many SLSN I progenitors and play critical roles in their LC energetics and evolution. Intrinsic temporal variations of the central engine can also be a possible driver for LC undulations. Our papers (Papers I and II) have put the studies of SLSN I population on a solid statistical footing. The prospect for future progress lies with better modeling of the high-quality ZTF LCs.

We thank Dr. Weili Lin from Tsinghua University for useful discussions of CSM modeling of SLSN I LCs. This work is based on observations obtained with the Samuel Oschin Telescope 48 inch and the 60 inch Telescope at the Palomar Observatory as part of the Zwicky Transient Facility project. ZTF is supported by the National Science Foundation under grant No. AST-1440341 and a collaboration including Caltech, IPAC, the Weizmann Institute for Science, the Oskar Klein Center at Stockholm University, the University of Maryland,

<sup>23</sup> SN 2018kyt, SN 2019hge, SN 2019neq, SN 2019unb.

<sup>24</sup> SN 2018bym, SN 2018fcg, SN 2019ujb, SN 2019lsq.

the University of Washington (UW), Deutsches Elektronen-Synchrotron and Humboldt University, Los Alamos National Laboratories, the TANGO Consortium of Taiwan, the University of Wisconsin at Milwaukee, and Lawrence Berkeley National Laboratories. Operations are conducted by Caltech Optical Observatories (COO), IPAC, and UW. The SED machine is based upon work supported by the National Science Foundation under grant No. 1106171. The ZTF forced-photometry service was funded under the Heising-Simons Foundation grant No. 12540303 (PI: Graham).

The Liverpool Telescope is operated on the island of La Palma by Liverpool John Moores University in the Spanish Observatorio del Roque de los Muchachos of the Instituto de Astrofísica de Canarias with financial support from the UK Science and Technology Facilities Council. The Nordic Optical Telescope is owned in collaboration by the University of Turku and Aarhus University, and operated jointly by Aarhus University, the University of Turku, and the University of Oslo, representing Denmark, Finland, and Norway, the University of Iceland and Stockholm University at the Observatorio del Roque de los Muchachos, La Palma, Spain, of the Instituto de Astrofísica de Canarias. This research has made use of data obtained through the High Energy Astrophysics Science Archive Research Center Online Service, provided by the NASA/Goddard Space Flight Center. This work was supported by the GROWTH project funded by the National Science Foundation under grant No. 1545949.

Z.C. acknowledges support from the China Scholarship Council. T.K. acknowledges support from the Swedish National Space Agency and the Swedish Research Council. S.S. acknowledges support from the G.R.E.A.T research environment, funded by *Vetenskapsrådet*, the Swedish Research Council, project number 2016-06012. T.-W.C. acknowledges the EU Funding under Marie Skłodowska-Curie

grant H2020-MSCA-IF-2018-842471. A.G.-Y. acknowledges support from the EU via the European Research Council grant No. 725161, the Israeli Science Foundation through the excellence center of the George Washington University, an IMOS space infrastructure grant and the Binational US-Israeli Science Foundation/Transformative and the German-Israeli Science Foundation grants, as well as the André Deloro Institute for Advanced Research in Space and Optics, the Schwartz/Reisman Collaborative Science Program, and the Norman E Alexander Family M Foundation ULTRASAT Data Center Fund, Minerva, and Yeda-Sela. R.L. acknowledges support from a Marie Skłodowska-Curie Individual Fellowship within the Horizon 2020 European Union (EU) Framework Programme for Research and Innovation (H2020-MSCA-IF-2017-794467). The work of X.W. is supported by the National Natural Science Foundation of China (NSFC grants 12033003 and 11633002), the Major State Basic Research Development Program (grant 2016YFA0400803), the Scholar Program of Beijing Academy of Science and Technology (DZ:BS202002), and the Tencent XPLOER Prize.

*Software:* SESNSpectraLib (Bianco et al. 2016), Scikit-learn (Pedregosa et al. 2011), MOSFiT (Guillochon et al. 2018), dynesty (Speagle 2020).

## Appendix

### The Complete Information on the ZTF SLSN I Sample

Table A1 lists the velocities measured from spectra, as well as the spectral phase and the ionization lines.

Table A2 lists the key parameters and reduced  $\chi^2$  value of the Magnetar and CSM+Ni model.

In Figure A1, we compare the key parameters of the magnetar model with those from Nicholl et al. (2017b).

**Table A1**  
Spectral Velocities

Name	Phase (days)	Ion	Velocity ( $\text{km s}^{-1}$ )
SN 2018avk	−4.52	Fe II	$11100^{+500}_{-350}$
SN 2018don	−2.17	Fe II	$12350^{+520}_{-450}$
SN 2018don	−1.24	Fe II	$12600^{+640}_{-650}$
SN 2018don	33.23	Fe II	$4740^{+640}_{-530}$
SN 2018bgv	17.98	Fe II	$16790^{+180}_{-210}$
SN 2018bgv	26.32	Fe II	$12090^{+120}_{-150}$
SN 2018lzv	86.01	Fe II	$8180^{+740}_{-630}$
SN 2018lzv	101.35	Fe II	$8300^{+400}_{-350}$
SN 2018lzv	142.49	Fe II	$6700^{+600}_{-580}$

(This table is available in its entirety in machine-readable form.)

**Table A2**  
Modeling Parameters

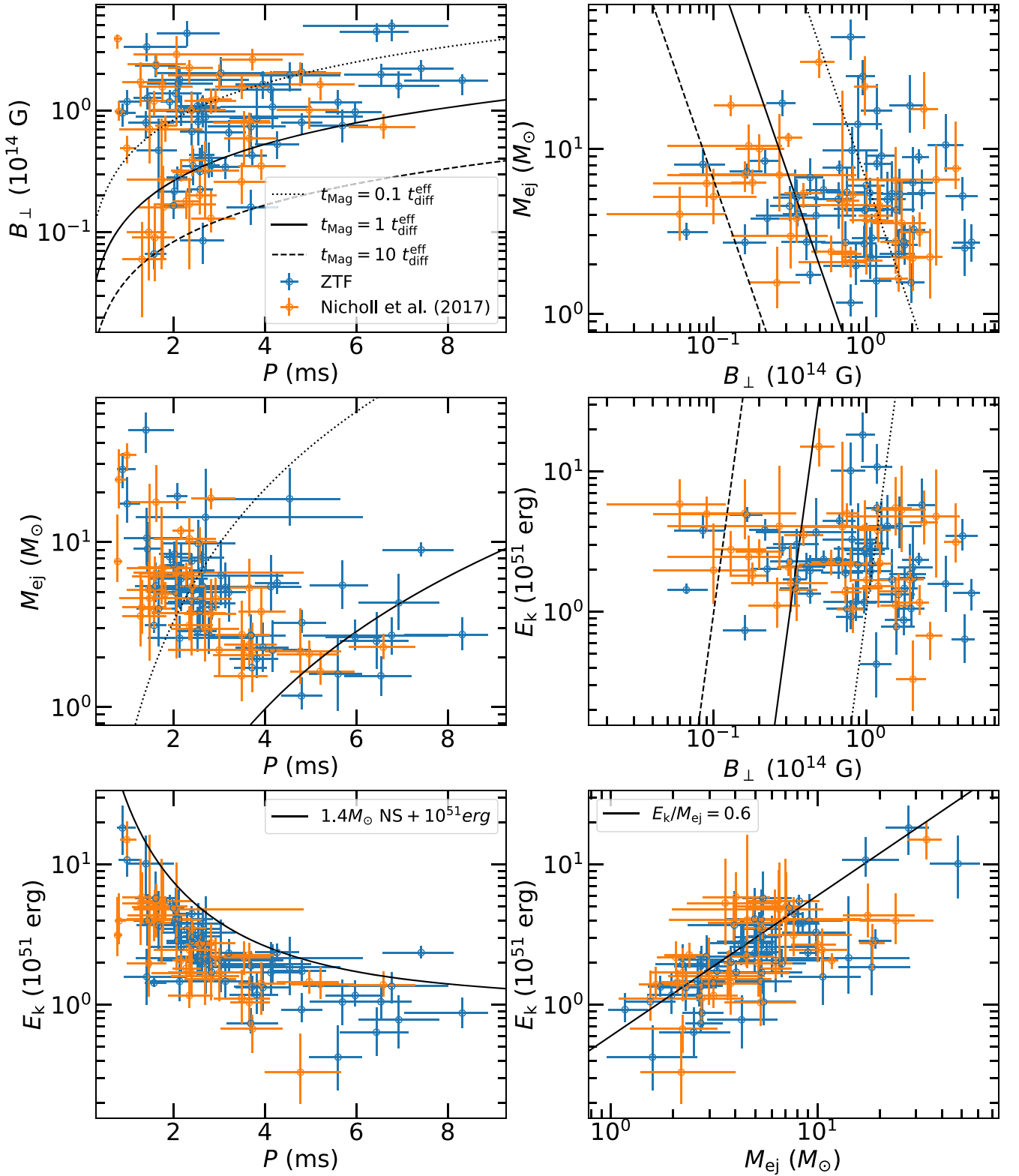
Name	Magnetar					$s$	CSM				
	$B_{\perp}$ ( $10^{14}$ G)	$P$ (ms)	$M_{\text{ej}}$ ( $M_{\odot}$ )	$V_{\text{ej}}$ ( $10^4$ km s $^{-1}$ )	$\chi^2/\text{dof}$		$M_{\text{Ni}}$ ( $M_{\odot}$ )	$M_{\text{CSM}}$ ( $M_{\odot}$ )	$M_{\text{ej}}$ ( $M_{\odot}$ )	$V_{\text{ej}}$ ( $10^4$ km s $^{-1}$ )	$\chi^2/\text{dof}$
SN 2018avk	$0.16^{+0.06}_{-0.05}$	$3.69^{+0.59}_{-0.53}$	$2.72^{+0.76}_{-0.42}$	$0.67^{+0.01}_{-0.00}$	1.38	0	$1.92^{+0.42}_{-0.38}$	$5.49^{+1.15}_{-1.02}$	$4.82^{+1.15}_{-0.89}$	$0.67^{+0.01}_{-0.00}$	1.50
SN 2018don	$1.11^{+0.20}_{-0.23}$	$4.60^{+0.59}_{-0.57}$	$10.74^{+0.84}_{-0.77}$	$0.76^{+0.00}_{-0.00}$	3.51	2	$3.37^{+0.27}_{-0.27}$	$0.63^{+0.32}_{-0.17}$	$40.78^{+3.02}_{-3.16}$	$1.04^{+0.03}_{-0.03}$	2.12
SN 2018bym	$1.18^{+0.28}_{-0.21}$	$1.92^{+0.23}_{-0.20}$	$8.16^{+0.93}_{-0.64}$	$1.06^{+0.02}_{-0.02}$	3.74	0	$3.41^{+0.19}_{-0.17}$	$3.94^{+0.36}_{-0.32}$	$26.69^{+2.02}_{-1.71}$	$1.06^{+0.02}_{-0.02}$	3.68
SN 2018bgv	$3.03^{+0.70}_{-0.53}$	$2.69^{+0.61}_{-0.48}$	$1.37^{+0.54}_{-0.34}$	$1.09^{+0.04}_{-0.03}$	39.30	0	$1.24^{+0.19}_{-0.09}$	$0.20^{+0.25}_{-0.07}$	$3.18^{+0.66}_{-0.48}$	$1.58^{+0.04}_{-0.05}$	9.65
SN 2018lzu	$0.95^{+0.18}_{-0.22}$	$0.89^{+0.28}_{-0.12}$	$27.62^{+6.84}_{-6.35}$	$1.04^{+0.12}_{-0.11}$	2.55	0	$0.35^{+0.91}_{-0.25}$	$13.35^{+5.36}_{-3.91}$	$52.14^{+21.31}_{-24.38}$	$1.07^{+0.14}_{-0.14}$	2.58
SN 2018gbw	$1.00^{+0.42}_{-0.39}$	$2.40^{+0.42}_{-0.52}$	$4.36^{+1.85}_{-2.11}$	$1.03^{+0.07}_{-0.06}$	2.71	2	$0.10^{+1.51}_{-1.36}$	$6.06^{+2.76}_{-1.44}$	$8.02^{+28.67}_{-6.52}$	$1.22^{+0.11}_{-0.12}$	2.84
SN 2018fcg	$4.92^{+0.65}_{-1.20}$	$6.77^{+1.23}_{-1.94}$	$2.73^{+0.76}_{-0.65}$	$0.91^{+0.03}_{-0.03}$	1.72	2	$0.58^{+0.06}_{-0.12}$	$1.97^{+0.38}_{-0.68}$	$1.91^{+0.91}_{-0.60}$	$0.95^{+0.12}_{-0.04}$	2.53
SN 2018gft	$0.17^{+0.04}_{-0.04}$	$2.00^{+0.23}_{-0.23}$	$7.30^{+0.84}_{-0.65}$	$1.06^{+0.03}_{-0.03}$	5.16	2	$0.01^{+0.03}_{-0.01}$	$18.83^{+2.74}_{-2.07}$	$0.22^{+0.13}_{-0.08}$	$1.28^{+0.04}_{-0.03}$	10.39
SN 2018lzx	$0.28^{+0.06}_{-0.06}$	$2.09^{+0.21}_{-0.23}$	$19.00^{+3.81}_{-3.12}$	$0.51^{+0.02}_{-0.02}$	1.40	0	$24.35^{+3.15}_{-4.04}$	$22.30^{+5.25}_{-3.83}$	$95.95^{+2.84}_{-6.32}$	$0.63^{+0.03}_{-0.02}$	1.80
SN 2018hpq	$1.58^{+0.50}_{-0.33}$	$6.93^{+0.88}_{-0.88}$	$4.29^{+2.12}_{-1.35}$	$0.55^{+0.04}_{-0.04}$	2.52	0	$0.01^{+0.02}_{-0.00}$	$9.84^{+3.39}_{-3.00}$	$1.35^{+4.12}_{-0.92}$	$0.54^{+0.03}_{-0.03}$	1.69
SN 2018lfe	$1.63^{+0.45}_{-0.40}$	$3.96^{+0.55}_{-0.60}$	$2.31^{+0.94}_{-0.67}$	$0.98^{+0.10}_{-0.10}$	0.54	2	$1.51^{+2.03}_{-1.36}$	$1.63^{+0.89}_{-0.42}$	$19.64^{+21.98}_{-14.89}$	$1.35^{+0.15}_{-0.12}$	1.25
SN 2018hti	$0.35^{+0.06}_{-0.07}$	$2.84^{+0.17}_{-0.28}$	$4.04^{+0.91}_{-0.61}$	$0.84^{+0.01}_{-0.00}$	12.30	0	$3.10^{+0.51}_{-0.53}$	$18.39^{+3.31}_{-3.02}$	$24.62^{+14.31}_{-10.50}$	$0.92^{+0.02}_{-0.02}$	18.77
SN 2018lfd	$1.26^{+0.31}_{-0.24}$	$1.43^{+0.33}_{-0.24}$	$9.10^{+4.15}_{-2.51}$	$0.85^{+0.07}_{-0.07}$	1.17	0	$2.99^{+0.62}_{-0.49}$	$5.41^{+0.92}_{-1.92}$	$49.08^{+3.49}_{-12.08}$	$0.92^{+0.06}_{-0.10}$	1.16
SN 2018kyt	$1.32^{+0.22}_{-0.28}$	$9.05^{+0.73}_{-1.01}$	$2.03^{+0.05}_{-0.61}$	$0.65^{+0.03}_{-0.02}$	6.36	2	$2.30^{+0.14}_{-0.10}$	$1.51^{+0.27}_{-0.23}$	$11.92^{+1.01}_{-1.23}$	$0.66^{+0.03}_{-0.02}$	4.03
SN 2019J	$3.33^{+1.01}_{-0.80}$	$1.42^{+0.86}_{-0.50}$	$10.60^{+5.57}_{-3.31}$	$0.50^{+0.05}_{-0.05}$	3.75	0	$0.18^{+0.18}_{-0.10}$	$6.26^{+2.10}_{-1.88}$	$33.42^{+10.78}_{-8.57}$	$0.43^{+0.04}_{-0.03}$	2.84
SN 2019cca	$1.00^{+0.32}_{-0.25}$	$2.17^{+0.57}_{-0.70}$	$6.03^{+3.67}_{-2.21}$	$0.87^{+0.09}_{-0.08}$	0.77	0	$0.80^{+2.60}_{-0.67}$	$10.96^{+5.73}_{-6.23}$	$28.16^{+24.14}_{-12.11}$	$0.85^{+0.15}_{-0.12}$	0.84
SN 2019bgu	$4.30^{+1.07}_{-0.97}$	$2.30^{+0.71}_{-0.66}$	$5.21^{+1.52}_{-0.98}$	$1.05^{+0.04}_{-0.02}$	1.74	2	$0.26^{+0.26}_{-0.23}$	$1.42^{+0.60}_{-0.32}$	$2.01^{+9.26}_{-1.52}$	$1.09^{+0.06}_{-0.05}$	1.89
SN 2019kwq	$0.43^{+0.09}_{-0.09}$	$2.63^{+0.27}_{-0.28}$	$6.73^{+2.04}_{-1.47}$	$0.70^{+0.04}_{-0.03}$	1.19	0	$22.04^{+1.50}_{-1.08}$	$11.47^{+1.95}_{-1.76}$	$78.56^{+9.65}_{-9.29}$	$0.71^{+0.03}_{-0.03}$	1.06
SN 2019dgr	$0.98^{+0.34}_{-0.26}$	$2.64^{+0.71}_{-0.79}$	$4.26^{+1.80}_{-1.25}$	$1.05^{+0.10}_{-0.09}$	1.79	0	$0.10^{+0.48}_{-0.07}$	$4.00^{+1.17}_{-0.71}$	$14.44^{+4.18}_{-3.90}$	$1.13^{+0.10}_{-0.08}$	1.66
SN 2019kws	$1.76^{+0.20}_{-0.44}$	$8.32^{+0.56}_{-1.27}$	$2.76^{+0.73}_{-0.54}$	$0.73^{+0.03}_{-0.03}$	1.62	2	$0.02^{+1.36}_{-0.02}$	$3.75^{+0.36}_{-0.99}$	$0.17^{+3.54}_{-0.05}$	$0.78^{+0.03}_{-0.06}$	1.49
SN 2019cdt	$2.95^{+0.94}_{-0.85}$	$1.49^{+0.58}_{-0.44}$	$5.27^{+1.88}_{-1.34}$	$1.55^{+0.13}_{-0.13}$	7.57	2	$0.00^{+0.06}_{-0.00}$	$2.52^{+0.59}_{-0.24}$	$0.59^{+17.33}_{-0.40}$	$1.55^{+0.08}_{-0.12}$	4.57
SN 2019aamp	$0.41^{+0.13}_{-0.13}$	$2.77^{+0.41}_{-0.32}$	$2.73^{+0.80}_{-0.62}$	$1.16^{+0.07}_{-0.12}$	0.84	0	$0.12^{+0.79}_{-0.09}$	$6.11^{+2.37}_{-2.91}$	$4.61^{+12.50}_{-2.01}$	$1.36^{+0.06}_{-0.09}$	0.96
SN 2019dlr	$1.48^{+0.60}_{-0.29}$	$4.13^{+0.66}_{-1.44}$	$5.37^{+3.03}_{-1.49}$	$0.73^{+0.06}_{-0.06}$	2.01	0	$0.64^{+1.18}_{-0.51}$	$3.24^{+0.43}_{-0.43}$	$32.49^{+12.05}_{-5.99}$	$0.76^{+0.04}_{-0.05}$	1.95
SN 2019cwu	$0.80^{+0.15}_{-0.16}$	$4.80^{+0.46}_{-0.44}$	$1.17^{+0.34}_{-0.20}$	$1.15^{+0.03}_{-0.03}$	1.09	0	$0.11^{+0.27}_{-0.10}$	$3.03^{+1.97}_{-1.63}$	$2.17^{+1.12}_{-1.63}$	$1.28^{+0.06}_{-0.05}$	1.12
SN 2019kwt	$0.20^{+0.05}_{-0.04}$	$1.80^{+0.29}_{-0.26}$	$12.01^{+1.58}_{-1.40}$	$0.83^{+0.04}_{-0.04}$	2.02	0	$0.30^{+1.96}_{-0.26}$	$20.02^{+5.63}_{-3.42}$	$20.69^{+6.62}_{-14.30}$	$0.73^{+0.04}_{-0.04}$	0.79
SN 2019eot	$0.67^{+0.18}_{-0.15}$	$2.40^{+0.27}_{-0.25}$	$7.70^{+0.84}_{-0.75}$	$0.98^{+0.02}_{-0.02}$	4.27	0	$0.30^{+0.69}_{-0.22}$	$4.55^{+0.43}_{-0.38}$	$26.31^{+2.43}_{-1.84}$	$1.09^{+0.02}_{-0.02}$	12.38
SN 2019kqu	$1.09^{+0.31}_{-0.29}$	$2.53^{+0.41}_{-0.47}$	$2.90^{+1.17}_{-0.72}$	$1.14^{+0.03}_{-0.05}$	0.61	0	$0.18^{+1.11}_{-0.15}$	$6.28^{+1.71}_{-1.10}$	$16.59^{+8.80}_{-5.49}$	$1.15^{+0.03}_{-0.04}$	0.65
SN 2019gqi	$0.73^{+0.21}_{-0.23}$	$3.70^{+0.76}_{-0.94}$	$2.72^{+0.94}_{-0.70}$	$1.07^{+0.07}_{-0.07}$	0.66	0	$0.52^{+1.98}_{-0.49}$	$3.38^{+3.05}_{-1.89}$	$11.37^{+14.66}_{-9.43}$	$1.14^{+0.13}_{-0.08}$	0.64
SN 2019fiy	$0.47^{+0.39}_{-0.28}$	$1.68^{+0.41}_{-0.48}$	$3.96^{+2.80}_{-1.61}$	$1.29^{+0.19}_{-0.18}$	2.95	0	$0.05^{+0.32}_{-0.04}$	$6.60^{+2.95}_{-2.00}$	$2.71^{+4.90}_{-1.87}$	$2.24^{+0.17}_{-0.29}$	3.76
SN 2019gam	$0.88^{+0.38}_{-0.43}$	$2.70^{+3.44}_{-1.52}$	$14.16^{+13.53}_{-7.60}$	$0.55^{+0.10}_{-0.09}$	1.86	0	$0.03^{+0.12}_{-0.02}$	$14.36^{+3.82}_{-3.07}$	$2.17^{+3.51}_{-1.23}$	$0.70^{+0.09}_{-0.08}$	2.08
SN 2019gfm	$1.97^{+0.43}_{-0.40}$	$6.54^{+0.67}_{-0.80}$	$1.55^{+0.49}_{-0.38}$	$1.07^{+0.04}_{-0.03}$	2.15	0	$0.02^{+0.17}_{-0.02}$	$2.16^{+0.67}_{-0.49}$	$0.89^{+1.04}_{-0.53}$	$1.16^{+0.06}_{-0.08}$	2.92
SN 2019hgo	$2.21^{+0.37}_{-0.48}$	$7.42^{+0.71}_{-0.84}$	$8.98^{+0.98}_{-0.81}$	$0.66^{+0.01}_{-0.00}$	9.03	2	$0.00^{+0.01}_{-0.00}$	$6.20^{+0.50}_{-0.39}$	$0.12^{+0.02}_{-0.01}$	$0.66^{+0.01}_{-0.00}$	6.65
SN 2019hne	$2.06^{+0.37}_{-0.35}$	$4.81^{+0.53}_{-0.62}$	$3.26^{+0.60}_{-0.44}$	$0.94^{+0.04}_{-0.04}$	1.41	0	$2.13^{+0.30}_{-0.27}$	$2.01^{+1.02}_{-0.23}$	$8.58^{+1.02}_{-0.75}$	$0.88^{+0.03}_{-0.03}$	1.09
SN 2019aamq	$0.22^{+0.05}_{-0.05}$	$2.02^{+0.39}_{-0.33}$	$8.47^{+1.64}_{-1.35}$	$0.86^{+0.02}_{-0.01}$	1.60	2	$0.57^{+2.68}_{-0.48}$	$22.39^{+4.09}_{-3.81}$	$9.45^{+39.94}_{-7.54}$	$0.87^{+0.03}_{-0.02}$	1.46
SN 2019kcy	$0.35^{+0.14}_{-0.11}$	$2.43^{+0.29}_{-0.28}$	$5.10^{+1.48}_{-1.22}$	$0.99^{+0.05}_{-0.05}$	0.57	2	$0.01^{+0.05}_{-0.01}$	$13.01^{+3.71}_{-2.76}$	$0.54^{+1.03}_{-0.32}$	$1.36^{+0.08}_{-0.07}$	1.00
SN 2019aamx	$0.81^{+0.38}_{-0.29}$	$2.54^{+0.80}_{-0.77}$	$9.83^{+3.85}_{-3.10}$	$0.76^{+0.07}_{-0.05}$	0.58	0	$1.67^{+3.18}_{-1.19}$	$4.04^{+1.21}_{-0.69}$	$57.51^{+11.87}_{-10.94}$	$0.78^{+0.04}_{-0.04}$	0.39
SN 2019aamr	$1.07^{+0.42}_{-0.37}$	$4.17^{+0.85}_{-1.13}$	$2.22^{+1.13}_{-0.58}$	$1.19^{+0.10}_{-0.10}$	0.73	2	$0.02^{+0.09}_{-0.01}$	$3.61^{+1.30}_{-0.60}$	$0.30^{+0.53}_{-0.16}$	$1.38^{+0.12}_{-0.10}$	0.71
SN 2019lsq	$0.97^{+0.19}_{-0.20}$	$5.98^{+0.58}_{-0.64}$	$2.67^{+0.74}_{-0.44}$	$0.85^{+0.01}_{-0.00}$	7.50	0	$0.03^{+0.13}_{-0.02}$	$6.39^{+1.79}_{-0.96}$	$1.00^{+0.58}_{-0.54}$	$0.86^{+0.01}_{-0.01}$	9.38
SN 2019nhs	$1.49^{+0.35}_{-0.29}$	$3.82^{+0.47}_{-0.43}$	$3.91^{+0.70}_{-0.47}$	$0.94^{+0.02}_{-0.01}$	3.28	2	$0.36^{+0.30}_{-0.30}$	$3.60^{+0.44}_{-0.27}$	$19.23^{+4.38}_{-16.27}$	$0.95^{+0.05}_{-0.02}$	1.70
SN 2019aams	$1.38^{+0.44}_{-0.35}$	$2.05^{+0.57}_{-0.62}$	$4.96^{+2.32}_{-1.37}$	$1.19^{+0.12}_{-0.10}$	1.09	0	$1.56^{+4.40}_{-1.41}$	$2.42^{+4.38}_{-0.67}$	$16.66^{+9.72}_{-13.88}$	$1.32^{+0.30}_{-0.10}$	0.94
SN 2019neq	$0.43^{+0.08}_{-0.08}$	$3.72^{+0.33}_{-0.38}$	$1.74^{+0.29}_{-0.22}$	$1.13^{+0.03}_{-0.03}$	13.07	0	$0.56^{+1.13}_{-0.22}$	$2.03^{+0.18}_{-0.28}$	$1.29^{+2.45}_{-0.49}$	$1.29^{+0.05}_{-0.05}$	14.31
SN 2019sgg	$1.18^{+0.29}_{-0.26}$	$0.99^{+0.28}_{-0.19}$	$17.09^{+7.58}_{-3.95}$	$1.02^{+0.03}_{-0.02}$	1.51	0	$1.99^{+8.22}_{-1.77}$	$4.21^{+0.69}_{-0.62}$	$56.15^{+6.22}_{-5.49}$	$1.03^{+0.03}_{-0.02}$	1.04
SN 2019aamt	$1.17^{+0.30}_{-0.25}$	$5.60^{+0.53}_{-0.63}$	$1.59^{+1.03}_{-0.63}$	$0.67^{+0.07}_{-0.07}$	1.07	0	$0.20^{+1.34}_{-0.17}$	$4.41^{+1.76}_{-1.52}$	$12.10^{+6.30}_{-5.36}$	$0.75^{+0.07}_{-0.06}$	1.05
SN 2019sgh	$1.78^{+0.38}_{-0.32}$	$2.14^{+1.51}_{-0.70}$	$2.62^{+0.95}_{-0.62}$	$0.97^{+0.07}_{-0.06}$	1.43	0	$0.05^{+0.18}_{-0.04}$	$2.41^{+0.92}_{-0.51}$	$6.54^{+2.47}_{-2.65}$	$1.18^{+0.09}_{-0.11}$	1.60
SN 2019stc	$0.95^{+0.19}_{-0.17}$	$6.76^{+1.25}_{-1.03}$	$3.13^{+0.84}_{-0.72}$	$0.88^{+0.08}_{-0.07}$	2.25	0	$5.70^{+0.66}_{-0.57}$	$3.83^{+1.72}_{-1.77}$	$25.88^{+8.89}_{-6.87}$	$0.75^{+0.06}_{-0.04}$	1.24
SN 2019szu	$0.79^{+0.20}_{-0.20}$	$1.40^{+0.60}_{-0.39}$	$47.92^{+13.16}_{-12.98}$	$0.59^{+0.08}_{-0.07}$	2.58	0	$9.30^{+3.27}_{-3.65}$	$15.79^{+6.52}_{-22.03}$	$70.43^{+18.78}_{-4.07}$	$0.52^{+0.04}_{-0.03}$	4.73
SN 2019unb	$1.99^{+0.41}_{-0.42}$	$3.62^{+1.05}_{-0.80}$	$8.23^{+3.33}_{-1.93}$	$0.43^{+0.03}_{-0.03}$	24.62	0	$1.06^{+0.20}_{-0.12}$	$2.48^{+1.19}_{-0.62}$	$36.57^{+12.57}_{-6.67}$	$0.46^{+0.03}_{-0.03}$	14.40
SN 2019ujb	$2.26^{+0.53}_{-0.52}$	$0.96^{+0.25}_{-0.17}$	$21.09^{+7.08}_{-4.60}$	$1.07^{+0.05}_{-0.03}$	4.77	0	$0.05^{+0.11}_{-0.04}$	$5.31^{+0.66}_{-0.56}$	$0.69^{+0.40}_{-0.22}$	$1.05^{+0.03}_{-0.02}$	2.25
SN 2019xdy	$2.02^{+0.70}_{-0.42}$	$3.04^{+1.35}_{-1.39}$	$6.27^{+4.02}_{-2.12}$								



**Table A2**  
(Continued)











Name	Magnetar					$s$	CSM				
	$B_{\perp}$ ( $10^{14}$ G)	$P$ (ms)	$M_{\text{ej}}$ ( $M_{\odot}$ )	$V_{\text{ej}}$ ( $10^4$ km s $^{-1}$ )	$\chi^2/dof$		$M_{\text{Ni}}$ ( $M_{\odot}$ )	$M_{\text{CSM}}$ ( $M_{\odot}$ )	$M_{\text{ej}}$ ( $M_{\odot}$ )	$V_{\text{ej}}$ ( $10^4$ km s $^{-1}$ )	$\chi^2/dof$
SN 2020dlb	$0.15^{+0.04}_{-0.03}$	$1.54^{+0.19}_{-0.18}$	$6.76^{+0.79}_{-0.84}$	$1.46^{+0.02}_{-0.01}$	4.79	2	$0.02^{+0.21}_{-0.02}$	$12.72^{+3.06}_{-3.26}$	$0.75^{+2.34}_{-0.46}$	$1.48^{+0.04}_{-0.02}$	2.59
SN 2020fyq	$1.94^{+0.33}_{-0.52}$	$4.54^{+1.11}_{-1.85}$	$18.34^{+9.79}_{-5.67}$	$0.41^{+0.02}_{-0.03}$	1.35	0	$0.13^{+0.27}_{-0.07}$	$7.85^{+1.50}_{-1.47}$	$44.23^{+6.50}_{-4.47}$	$0.35^{+0.01}_{-0.01}$	1.24
SN 2020exj	$4.44^{+0.71}_{-0.78}$	$6.44^{+0.70}_{-0.79}$	$2.51^{+1.25}_{-0.80}$	$0.65^{+0.02}_{-0.02}$	1.67	2	$0.04^{+0.04}_{-0.02}$	$1.62^{+0.25}_{-0.20}$	$21.53^{+2.49}_{-2.38}$	$0.70^{+0.03}_{-0.03}$	2.11
SN 2020htd	$0.41^{+0.08}_{-0.09}$	$3.79^{+0.35}_{-0.43}$	$6.69^{+2.93}_{-1.81}$	$0.52^{+0.05}_{-0.05}$	5.21	0	$3.05^{+1.10}_{-1.00}$	$10.89^{+1.28}_{-1.27}$	$94.86^{+3.43}_{-5.92}$	$0.48^{+0.02}_{-0.02}$	1.71
SN 2020iyj	$0.66^{+0.17}_{-0.20}$	$3.21^{+0.37}_{-0.67}$	$4.97^{+1.33}_{-1.67}$	$0.90^{+0.06}_{-0.06}$	1.26	0	$1.09^{+1.56}_{-0.76}$	$9.87^{+3.40}_{-3.84}$	$15.68^{+12.34}_{-8.28}$	$0.91^{+0.11}_{-0.08}$	1.28
SN 2020kox	$0.22^{+0.05}_{-0.05}$	$2.58^{+0.27}_{-0.29}$	$3.81^{+1.17}_{-0.87}$	$0.93^{+0.10}_{-0.05}$	2.25	0	$0.56^{+11.36}_{-0.50}$	$19.06^{+5.76}_{-10.70}$	$22.10^{+34.95}_{-15.16}$	$0.97^{+0.16}_{-0.08}$	2.99
SN 2020jii	$1.06^{+0.23}_{-0.21}$	$2.63^{+0.40}_{-0.41}$	$5.43^{+1.27}_{-0.89}$	$0.97^{+0.04}_{-0.05}$	1.35	0	$6.61^{+1.24}_{-1.31}$	$2.82^{+0.45}_{-0.38}$	$21.65^{+3.46}_{-2.61}$	$1.09^{+0.04}_{-0.05}$	1.25
SN 2020afah	$0.07^{+0.03}_{-0.02}$	$1.58^{+0.26}_{-0.20}$	$3.13^{+0.43}_{-0.32}$	$0.88^{+0.04}_{-0.04}$	1.15	0	$7.18^{+2.34}_{-2.64}$	$11.02^{+3.86}_{-3.10}$	$20.65^{+6.49}_{-4.20}$	$0.98^{+0.05}_{-0.06}$	1.03
SN 2020afag	$0.85^{+0.13}_{-0.16}$	$3.58^{+0.34}_{-0.38}$	$4.82^{+1.01}_{-0.76}$	$0.84^{+0.04}_{-0.04}$	1.98	0	$12.60^{+1.12}_{-1.03}$	$4.67^{+1.12}_{-7.55}$	$42.84^{+7.68}_{-7.55}$	$0.87^{+0.04}_{-0.04}$	1.21
SN 2020onb	$0.53^{+0.15}_{-0.12}$	$4.27^{+0.47}_{-0.48}$	$5.67^{+0.85}_{-0.77}$	$0.83^{+0.02}_{-0.01}$	2.50	0	$0.04^{+0.16}_{-0.03}$	$8.39^{+2.51}_{-1.75}$	$0.77^{+0.87}_{-0.43}$	$0.84^{+0.03}_{-0.02}$	2.46
SN 2020qef	$1.13^{+0.22}_{-0.24}$	$8.45^{+0.77}_{-0.94}$	$2.82^{+1.26}_{-0.77}$	$0.65^{+0.04}_{-0.04}$	4.12	2	$3.16^{+0.18}_{-0.18}$	$2.23^{+0.29}_{-0.27}$	$10.49^{+1.40}_{-1.18}$	$0.61^{+0.02}_{-0.02}$	0.80
SN 2020rmv	$0.34^{+0.07}_{-0.07}$	$3.14^{+0.32}_{-0.33}$	$5.32^{+2.20}_{-1.33}$	$0.68^{+0.03}_{-0.03}$	3.19	2	$0.02^{+0.13}_{-0.01}$	$16.71^{+4.04}_{-3.41}$	$1.70^{+3.08}_{-1.01}$	$0.90^{+0.05}_{-0.04}$	4.82
SN 2020xkv	$0.09^{+0.03}_{-0.03}$	$2.65^{+0.45}_{-0.50}$	$8.09^{+2.08}_{-1.00}$	$0.89^{+0.03}_{-0.03}$	1.04	0	$0.00^{+0.03}_{-0.00}$	$29.43^{+0.39}_{-0.73}$	$0.14^{+0.05}_{-0.03}$	$0.82^{+0.02}_{-0.03}$	1.11
SN 2020xgd	$1.66^{+0.65}_{-0.46}$	$2.11^{+0.74}_{-0.69}$	$5.33^{+2.27}_{-1.30}$	$1.14^{+0.09}_{-0.07}$	1.14	2	$1.13^{+3.77}_{-1.10}$	$3.89^{+1.58}_{-0.65}$	$7.31^{+12.12}_{-5.90}$	$1.16^{+0.08}_{-0.07}$	0.93

(This table is available in its entirety in machine-readable form.)



**Figure A1.** Values and  $1\sigma$  errors of key parameters ( $P$ ,  $B_{\perp}$ ,  $M_{\text{ej}}$ ,  $E_k$ ) for the 7 SLSNe I favored by magnetar models and the 47 equally well-fit ones. The values from our sample are marked in blue while those from Nicholl et al. (2017b) are marked in orange.  $t_{\text{mag}}$  is the spin-down timescale for the magnetar model, and the ratio of  $t_{\text{mag}}/t_{\text{diff}}^{\text{eff}}$  follows (Nicholl et al. 2017b, their Equation (11)).

## ORCID iDs

Z. H. Chen  <https://orcid.org/0000-0001-5175-4652>  
 Lin Yan  <https://orcid.org/0000-0003-1710-9339>  
 T. Kangas  <https://orcid.org/0000-0002-5477-0217>  
 R. Lunnan  <https://orcid.org/0000-0001-9454-4639>  
 J. Sollerman  <https://orcid.org/0000-0003-1546-6615>  
 S. Schulze  <https://orcid.org/0000-0001-6797-1889>  
 D. A. Perley  <https://orcid.org/0000-0001-8472-1996>  
 T.-W. Chen  <https://orcid.org/0000-0002-1066-6098>  
 A. Gal-Yam  <https://orcid.org/0000-0002-3653-5598>  
 X. F. Wang  <https://orcid.org/0000-0002-7334-2357>  
 E. Bellm  <https://orcid.org/0000-0001-8018-5348>  
 J. S. Bloom  <https://orcid.org/0000-0002-7777-216X>  
 R. Dekany  <https://orcid.org/0000-0002-5884-7867>  
 M. Graham  <https://orcid.org/0000-0002-3168-0139>  
 M. Kasliwal  <https://orcid.org/0000-0002-5619-4938>  
 S. Kulkarni  <https://orcid.org/0000-0001-5390-8563>  
 R. Laher  <https://orcid.org/0000-0003-2451-5482>  
 B. Rusholme  <https://orcid.org/0000-0001-7648-4142>

## References

- Anderson, J. P., Pessi, P. J., Dessart, L., et al. 2018, *A&A*, **620**, A67  
 Angus, C. R., Smith, M., Sullivan, M., et al. 2019, *MNRAS*, **487**, 2215  
 Arnett, W. D. 1982, *ApJ*, **253**, 785  
 Barkat, Z., Rakavy, G., & Sack, N. 1967, *PhRvL*, **18**, 379  
 Bellm, E. C., Kulkarni, S. R., Barlow, T., et al. 2019b, *PASP*, **131**, 068003  
 Bellm, E. C., Kulkarni, S. R., Graham, M. J., et al. 2019a, *PASP*, **131**, 018002  
 Benetti, S., Nicholl, M., Cappellaro, E., et al. 2014, *MNRAS*, **441**, 289  
 Bianco, F. B., Liu, Y. Q., & Modjaz, M. 2016, SESNSpectraLib: First Public Release, v1.0, Zenodo, doi:10.5281/zenodo.58767  
 Blanchard, P. K., Berger, E., Nicholl, M., & Villar, V. A. 2020, *ApJ*, **897**, 114  
 Bressan, A., Marigo, P., Girardi, L., et al. 2012, *MNRAS*, **427**, 127  
 Chatzopoulos, E., Wheeler, J. C., & Vinko, J. 2012, *ApJ*, **746**, 121  
 Chatzopoulos, E., Wheeler, J. C., Vinko, J., Horvath, Z. L., & Nagy, A. 2013, *ApJ*, **773**, 76  
 Chen, K.-J., Woosley, S. E., & Whalen, D. J. 2020, *ApJ*, **893**, 99  
 Chen, Z. H., Yan, L., Kangas, T., et al. 2022, arXiv:2202.02059  
 Chevalier, R. A., & Irwin, C. M. 2011, *ApJL*, **729**, L6  
 De Cia, A., Gal-Yam, A., Rubin, A., et al. 2018, *ApJ*, **860**, 100  
 Dessart, L. 2019, *A&A*, **621**, A141  
 Dessart, L., Hillier, D. J., Waldman, R., Livne, E., & Blondin, S. 2012, *MNRAS Lett.*, **426**, L76  
 Dexter, J., & Kasen, D. 2013, *ApJ*, **772**, 30  
 Gal-Yam, A. 2019, *ApJ*, **882**, 102  
 Gehrels, N. 1986, *ApJ*, **303**, 336  
 Graham, M. J., Kulkarni, S. R., Bellm, E. C., et al. 2019, *PASP*, **131**, 078001  
 Guillochon, J., Nicholl, M., Villar, V. A., et al. 2018, *ApJS*, **236**, 6  
 Hosseinzadeh, G., Berger, E., Metzger, B. D., et al. 2022, *ApJ*, **933**, 14  
 Hsu, B., Hosseinzadeh, G., & Berger, E. 2021, *ApJ*, **921**, 180  
 Inserra, C. 2019, *NatAs*, **3**, 697  
 Inserra, C., Smartt, S. J., Jerkstrand, A., et al. 2013, *ApJ*, **770**, 128  
 Jiang, B., Jiang, S., & Ashley Villar, V. 2020, *RNAAS*, **4**, 16  
 Kaplan, N., & Soker, N. 2020, *MNRAS*, **494**, 5909  
 Kasen, D., & Bildsten, L. 2010, *ApJ*, **717**, 245  
 Kasen, D., Metzger, B. D., & Bildsten, L. 2016, *ApJ*, **821**, 36  
 Kasen, D., Woosley, S. E., & Heger, A. 2011, *ApJ*, **734**, 102  
 Lattimer, J. M., & Prakash, M. 2007, *PhR*, **442**, 109  
 Leloudas, G., Chatzopoulos, E., Dilday, B., et al. 2012, *A&A*, **541**, A129  
 Li, L., Wang, S.-Q., Liu, L.-D., et al. 2020, *ApJ*, **891**, 98  
 Liu, L.-D., Gao, H., Wang, X.-F., & Yang, S. 2021, *ApJ*, **911**, 142  
 Liu, L.-D., Wang, L.-J., Wang, S.-Q., & Dai, Z.-G. 2017a, arXiv:1706.01783  
 Liu, Y.-Q., Modjaz, M., & Bianco, F. B. 2017b, *ApJ*, **845**, 85  
 Liu, Y.-Q., Modjaz, M., Bianco, F. B., & Graur, O. 2016, *ApJ*, **827**, 90  
 Lunnan, R., Fransson, C., Vreeswijk, P. M., et al. 2018, *NatAs*, **2**, 887  
 Lunnan, R., Yan, L., Perley, D. A., et al. 2020, *ApJ*, **901**, 61  
 Lyman, J. D., Bersier, D., James, P. A., et al. 2016, *MNRAS*, **457**, 328  
 Margutti, R., Metzger, B. D., Chornock, R., et al. 2017, *ApJ*, **836**, 25  
 Masci, F. J., Laher, R. R., Rusholme, B., et al. 2019, *PASP*, **131**, 018003  
 Modjaz, M., Liu, Y. Q., Bianco, F. B., & Graur, O. 2016, *ApJ*, **832**, 108  
 Moriya, T. J., Blinnikov, S. I., Tominaga, N., et al. 2013, *MNRAS*, **428**, 1020  
 Moriya, T. J., & Maeda, K. 2012, *ApJL*, **756**, L22  
 Nicholl, M., Berger, E., Smartt, S. J., et al. 2016, *ApJ*, **826**, 39  
 Nicholl, M., Berger, E., Margutti, R., et al. 2017a, *ApJL*, **845**, L8  
 Nicholl, M., Guillochon, J., & Berger, E. 2017b, *ApJ*, **850**, 55  
 Nicholl, M., & Smartt, S. J. 2016, *MNRAS Lett.*, **457**, L79  
 Nicholl, M., Smartt, S. J., Jerkstrand, A., et al. 2013, *Natur*, **502**, 346  
 Nicholl, M., Smartt, S. J., Jerkstrand, A., et al. 2015a, *ApJL*, **807**, L18  
 Nicholl, M., Smartt, S. J., Jerkstrand, A., et al. 2015b, *MNRAS*, **452**, 3869  
 Nyholm, A., Sollerman, J., Tartaglia, L., et al. 2020, *A&A*, **637**, A73  
 Ofek, E. O., Cameron, P. B., Kasliwal, M. M., et al. 2007, *ApJL*, **659**, L13  
 Oke, J. B., Cohen, J. G., Carr, M., et al. 1995, *PASP*, **107**, 375  
 Oke, J. B., & Gunn, J. E. 1983, *ApJ*, **266**, 713  
 Pedregosa, F., Varoquaux, G., Gramfort, A., et al. 2011, *JMLR*, **12**, 2825  
 Piro, A. L. 2015, *ApJL*, **808**, L51  
 Prentice, S. J., Mazzali, P. A., Pian, E., et al. 2016, *MNRAS*, **458**, 2973  
 Quataert, E., Lecoanet, D., & Coughlin, E. R. 2019, *MNRAS Lett.*, **485**, L83  
 Quimby, R. M., Aldering, G., Wheeler, J. C., et al. 2007, *ApJL*, **668**, L99  
 Quimby, R. M., De Cia, A., Gal-Yam, A., et al. 2018, *ApJ*, **855**, 2  
 Quimby, R. M., Kulkarni, S. R., Kasliwal, M. M., et al. 2011, *Natur*, **474**, 487  
 Rakavy, G., & Shaviv, G. 1967, *ApJ*, **148**, 803  
 Roming, P. W. A., Kennedy, T. E., Mason, K. O., et al. 2005, *SSRv*, **120**, 95  
 Ryder, S. D., Sadler, E. M., Subrahmanyam, R., et al. 2004, *MNRAS*, **349**, 1093  
 Smith, M., Sullivan, M., D'Andrea, C. B., et al. 2016, *ApJL*, **818**, L8  
 Smith, N., Li, W., Foley, R. J., et al. 2007, *ApJ*, **666**, 1116  
 Sorokina, E., Blinnikov, S., Nomoto, K., Quimby, R., & Tolstov, A. 2016, *ApJ*, **829**, 17  
 Speagle, J. S. 2020, *MNRAS*, **493**, 3132  
 Terreran, G., Blanchard, P., DeMarchi, L., et al. 2020, *ATel*, **13970**, 1  
 Villar, V. A., Berger, E., Metzger, B. D., & Guillochon, J. 2017, *ApJ*, **849**, 70  
 Vreeswijk, P. M., Leloudas, G., Gal-Yam, A., et al. 2017, *ApJ*, **835**, 58  
 Vurm, I., & Metzger, B. D. 2021, *ApJ*, **917**, 77  
 Wheeler, J. C., Chatzopoulos, E., Vinkó, J., & Tuminello, R. 2017, *ApJL*, **851**, L14  
 Woosley, S. E. 2010, *ApJL*, **719**, L204  
 Woosley, S. E. 2017, *ApJ*, **836**, 244  
 Woosley, S. E., Blinnikov, S., & Heger, A. 2007, *Natur*, **450**, 390  
 Yan, L., Lunnan, R., Perley, D. A., et al. 2017b, *ApJ*, **848**, 6  
 Yan, L., Perley, D. A., Schulze, S., et al. 2020, *ApJL*, **902**, L8  
 Yan, L., Quimby, R., Gal-Yam, A., et al. 2017a, *ApJ*, **840**, 57  
 Yan, L., Quimby, R., Ofek, E., et al. 2015, *ApJ*, **814**, 108